

1 **What caused record-breaking aerosol loading over the South China** 2 **Sea in April 2023**

3 **Saginya Ravindra Babu^{1*} and Neng-Huei Lin^{1,2*}**

4 ¹Department of Atmospheric Sciences, National Central University, Taoyuan 32001, Taiwan.

5 ²Center for Environmental Monitoring and Technology, National Central University, Taoyuan
6 32001, Taiwan.

7 Correspondence to: S. Ravindra Babu (baburavindra595@gmail.com) and Neng-Huei Lin
8 (nhlin@cc.ncu.edu.tw).

9 **Abstract:**

10 In April 2023, the South China Sea (SCS) experienced an unprecedented surge in aerosol loading,
11 with aerosol optical depth (AOD) reaching the highest levels recorded during the 2-decade period
12 of Moderate Resolution Imaging Spectroradiometer (MODIS) satellite data (2003–2023). AOD
13 increased by ~150% relative to the long-term mean (2002–2022), indicating an anomaly exceeding
14 4σ , and was accompanied by pronounced enhancement in carbon monoxide (CO) at 700 and 500
15 hPa. Using multi-sensor satellite measurements and MERRA-2 reanalysis, we investigated the
16 sources, driving mechanisms, and atmospheric dynamics behind this extreme aerosol event.
17 MODIS fire counts, burned-area data, and NOAA HYSPLIT back-trajectory analyses identify
18 intense biomass-burning (BB) across northern Peninsular Southeast Asia (PSEA) as the dominant
19 source, particularly from Laos and Myanmar. The BB was facilitated by anomalous meteorological
20 conditions associated with a persistent tropospheric anti-cyclonic anomaly over PSEA, which
21 suppressed convection and promoted subsidence, elevated surface temperatures, and led to
22 widespread drought. The dynamical large-scale circulation anomalies further revealed
23 substantially altered transport pathways. A coupled dynamical pattern involving a western North
24 Pacific (WNP) cyclone, a BoB anticyclone at 700 hPa, and a PSEA anticyclone at 500 hPa
25 generated persistent northerly flow over the SCS, redirecting smoke plumes southward toward the
26 SCS and southern BoB rather than along the climatological pathway toward Taiwan and the
27 northwestern Pacific. These findings reveal how the combined influence of extreme BB emissions
28 and anomalous circulation produced the record aerosol loading over the SCS, highlighting critical
29 links among BB emissions and atmospheric dynamics in shaping regional air quality extremes.

30 **Key words: Aerosol loading; South China Sea; MODIS; Biomass burning**

31 **1. Introduction**

32 Atmospheric aerosols play a vital role in Earth’s climate by impacting radiation balance, cloud
33 microphysics, and air quality (Ramanathan et al., 2001; Anderson et al., 2003; Forster et al., 2021;
34 IPCC, 2023). These particles scatter and absorb solar radiation directly, influencing radiative
35 effects, and also modify cloud properties, lifespan, and precipitation by serving as nuclei for
36 condensation and ice formation. As a result, aerosols affect atmospheric thermodynamics, cloud–
37 radiation interactions, and the water cycle (Twomey et al., 1977; IPCC, 2023). Monitoring aerosol
38 levels over remote ocean regions is especially important because these areas provide a baseline for
39 natural background aerosol levels and help evaluate the effects of long-range transport and their
40 influence on regional climate through radiative and cloud processes (Pani et al., 2023). In addition
41 to anthropogenic emissions, natural events such as wildfires and agricultural biomass burning are
42 significant episodic sources, emitting large quantities of aerosol particles and trace gases that
43 substantially affect both regional and global climate systems (Crutzen and Andreae, 1990;
44 Ramanathan et al., 2001; Lin et al., 2013; Reid et al., 2013; Kolden et al., 2024).

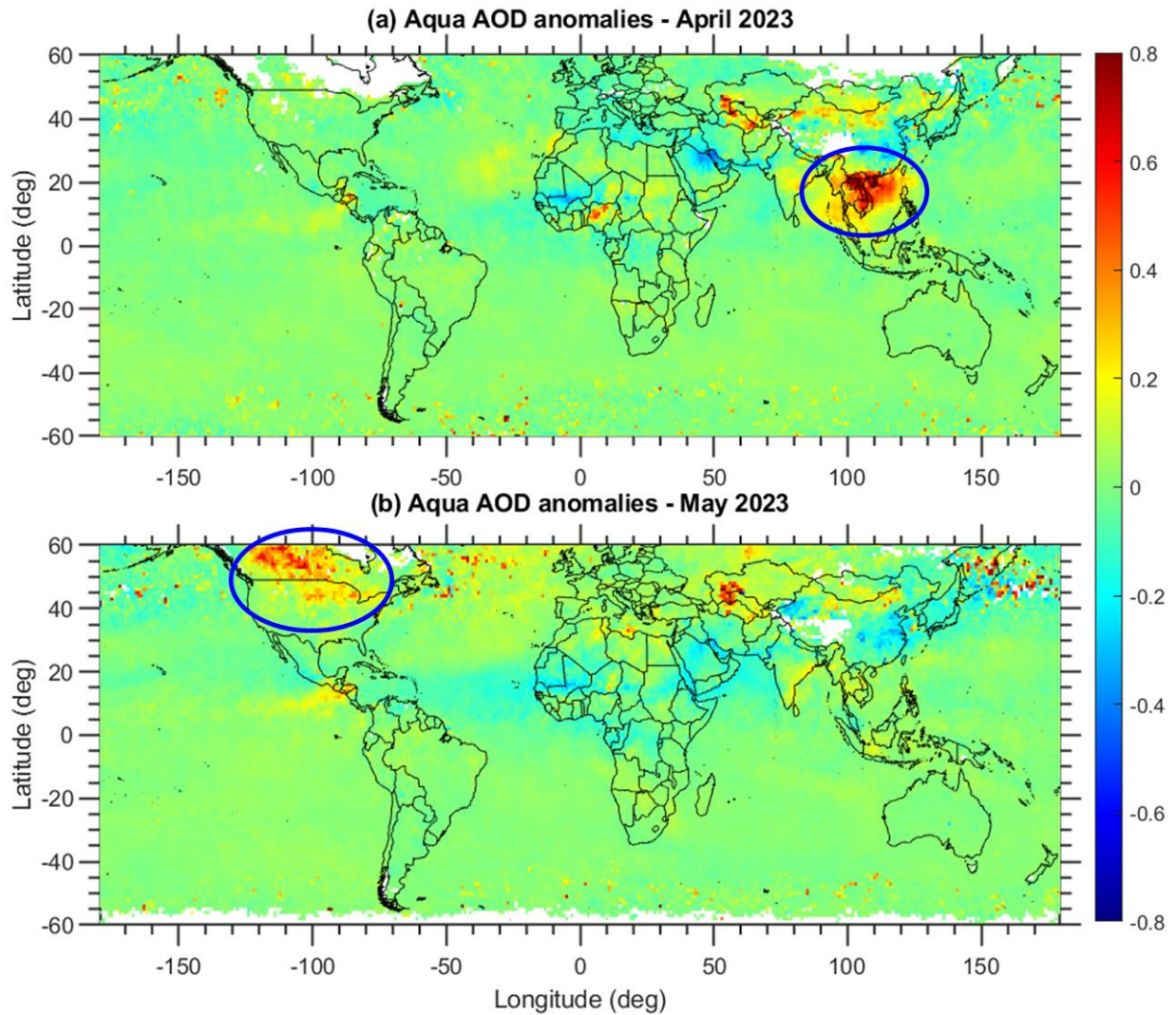
45 The South China Sea (SCS), situated in Asia, is the largest marginal sea in the tropical–
46 subtropical western North Pacific, serving as a vital natural laboratory for examining aerosol
47 variability in a relatively pristine marine environment (Reid et al., 2013; Lin et al., 2013; Pani et
48 al., 2023). Although it is an oceanic region, the atmosphere over the SCS is significantly influenced
49 by emissions from nearby continents and regional circulation patterns (Pani et al., 2023).
50 Typically, the SCS is dominated by a monsoon system, with the northeast monsoon occurring
51 during boreal winter and spring, and the southwest monsoon during boreal summer and autumn
52 (Cui et al., 2016). These seasonal wind patterns play a key role in aerosol transport, often carrying
53 natural and human-made pollutants from East Asia into the SCS basin over long distances. In
54 addition to continental outflow from East Asia, biomass-burning emissions from surrounding areas
55 notably influence aerosol concentrations over the SCS. During the summer monsoon months,
56 particularly August to October, persistent peatland and forest fires across the Maritime Continent
57 (MC) generate large smoke plumes that drift toward the southern SCS (Ravindra Babu et al., 2023).
58 Moreover, extensive open biomass burning in spring over Peninsular Southeast Asia (PSEA),
59 including Myanmar, Thailand, Cambodia, Laos, and Vietnam, serves as a key source of aerosols
60 affecting the SCS atmosphere (Chan et al., 2003; Ou-Yang et al., 2012; Yadav et al., 2017; Liao

61 et al., 2021; Wang et al., 2021; Pani et al., 2023; Wang et al., 2025). This region is recognized as
62 a global hotspot for biomass burning (Lin et al., 2013; Reid et al., 2013; Cohen, 2014; Cohen et
63 al., 2017; Pani et al., 2019), significantly contributing to carbon emissions and aerosol loading
64 during the peak fire season in March and April (Ravindra Babu and Lin, 2023). These fires mainly
65 stem from slash-and-burn farming practices occurring annually across PSEA (Lee et al., 2016;
66 Tsay et al., 2016; Huang et al., 2020), releasing substantial particulate matter and trace gases into
67 the air (Ou-Yang et al., 2022). As a result, aerosol variability in the SCS region is largely driven
68 by the interaction between regional emission sources and the prevailing monsoon circulation,
69 which influences aerosol transport, dispersion, and accumulation within the basin (Pani et al.,
70 2023).

71 The year 2023 saw exceptional wildfires worldwide due to record-high global mean surface
72 temperatures, which affected carbon emissions and aerosol levels (Esper et al., 2024; Forster et al.,
73 2024; Min, 2024; Raghuraman et al., 2024; Kolden et al., 2024; Liu et al., 2024; Byrne et al., 2024;
74 MacCarthy et al., 2024). It is reported that 70% of the total burning occurs in the Northern
75 Hemisphere (Kolden et al., 2024). Among all, Canadian wildfires emerged as the primary hotspot,
76 with significant fires in both the eastern and western regions causing notable increases in carbon
77 monoxide (CO) and tropospheric aerosols over the past twenty years (Liu et al., 2024; Byrne et
78 al., 2024; MacCarthy et al., 2024). Although the unprecedented Canadian wildfires in 2023
79 received considerable scientific attention and were well documented in several studies, the record-
80 breaking aerosol loading over the SCS in April 2023 attracted relatively little international
81 attention. The historic event over the SCS in April 2023 can be seen through the Moderate
82 Resolution Imaging Spectroradiometer (MODIS) Aqua AOD anomalies compared to the long-
83 term mean (2003-2022), which shows extreme positive anomalies over the SCS and surrounding
84 regions during that month, contrasting with the rest of the globe (**Fig. 1**). However, AOD
85 anomalies in May illustrate the absence of positive anomalies over the SCS and instead show
86 higher positive anomalies over North America, which are related to the Canadian wildfires. The
87 time series of monthly mean AOD over the SCS further confirms a record-high AOD in April 2023
88 relative to the MODIS data from 2003 to 2023 (**Fig. 2d**). The exceptional aerosol loading in April
89 2023 is unusual for remote marine locations such as the SCS and warrants further investigation.
90 In this study, we investigated the factors and physical processes that contributed to the
91 unprecedented aerosol levels observed in April 2023, using extensive data collected from multiple

92 sources over an extended period. The following three major topics are examined in detail within
93 this study:

- 94 • How extreme are these AOD anomalies, and what magnitude was increased?
- 95 • What are the sources for these record-breaking aerosol loadings over SCS?
- 96 • Were dynamic and large-scale circulations responsible for this event?



97
98 **Figure 1.** MODIS Aqua measured AOD anomalies in (a) April 2023 and (b) May 2023 compared
99 to the long-term mean (2003-2022). The highlighted circles in (a) and (b) indicate the AOD
100 anomalies over the South China Sea (SCS) and Canada regions. This figure highlights that the
101 AOD anomalies observed by MODIS are significant and particularly pronounced over the SCS
102 compared to the other areas globally. It illustrates the unique characteristics of April 2023
103 compared to long-term mean. Data visualizations produced using MATLAB 2023b
104 (<https://matlab.mathworks.com>).

105 **2. Data and Methodology**

106 **2.1 Data**

107 This study relies entirely on publicly available data, covering the period from 2003 to 2023. We
108 used data products from various satellite measurements, ground-based observations, and reanalysis
109 products.

110 **2.1.1 Satellite remote sensing measurements**

111 **Moderate Resolution Imaging Spectroradiometer (MODIS)**

112 MODIS is a passive sensor aboard the Aqua and Terra satellites, which are in a sun-synchronous
113 orbit, and pass the Equator in the morning (Aqua) and afternoon (Terra). From MODIS satellite
114 measurements, we utilized aerosol optical depth (AOD), fire counts, fire radiative power (FRP),
115 cloud fraction, and burned area products. We used Level 3 monthly AOD at $1^\circ \times 1^\circ$ spatial
116 resolution derived from the mean of the Dark Target and Deep Blue Combined Aerosol Products
117 from the Terra satellite (MOD08_M3 Collection 6.1) and Aqua satellite (MYD08_M3 Collection
118 6.1) (Platnick et al., 2015; Buchholz et al., 2020). For MODIS AOD, the estimated uncertainty is
119 approximately ± 0.05 over ocean and ± 0.15 over land. The Collection 6.1 (C6.1) products used in
120 this study have been shown to capture temporal variations effectively and agree closely with
121 ground-based observations (Wei et al., 2019a). Validation against AEROSOL ROBOTIC NETWORK
122 (AERONET) measurements demonstrates that the merged Dark Target and Deep Blue (DTB)
123 products accurately capture aerosol variability at both regional and global scales (Sayer et al.,
124 2014; Wei et al., 2019b). Additionally, we used MODIS's daily fire counts and fire radiative power
125 (FRP) products (Giglio et al., 2006, 2016, 2018). Direct fire counts from MODIS were obtained
126 from the Fire Information for Resource Management System (FIRMS) dataset. We selected all
127 MODIS fire counts from the Terra and Aqua sensors with a confidence level of at least 80%.
128 Finally, we utilized Cloud Fraction data from both the Terra and Aqua satellites.

129 **Measurements Of Pollution In The Troposphere (MOPITT)**

130 MOPITT is a multi-channel thermal infrared (TIR) and near-infrared (NIR) instrument operating
131 on board the sun-synchronous polar-orbiting NASA Terra satellite. This study uses a version 9
132 (MOP03TM_9) gridded monthly product (Worden et al., 2010; Deeter et al., 2019). For more

133 details on the retrieval algorithm, validation, and uncertainties in MOPITT CO, see Deeter et al.
134 (2019).

135 **Atmospheric Infrared Sounder (AIRS)**

136 In addition to the MOPITT measurements, we used CO from the AIRS instrument on the NASA
137 Aqua satellite, which provides CO at multiple vertical levels twice daily and has near-global
138 coverage. AIRS uses wavenumbers 2183–2200 cm⁻¹ (4.58–4.5 μm) for retrieving CO (McMillan
139 et al., 2005). The V9 level 3 CO product, available at 1° × 1° resolution at 700 and 500 hPa levels,
140 was utilized in the present study. AIRS sensitivity to CO is broad and optimal in the mid-
141 troposphere between approximately 300 and 600 hPa (Warner et al., 2007, 2013; AIRS project,
142 2019). CO retrievals exhibit a 6%–10 % bias between 900 and 300 hPa with a root mean square
143 error of 8%–12 % (McMillan et al., 2011). In addition to CO, we also utilized ozone, surface
144 temperature, and outgoing longwave radiation (OLR) data from the AIRS satellite.

145 **Global Precipitation Climatology Project (GPCP)**

146 The Global Precipitation Climatology Project (GPCP) Version 3.2 Satellite-Gauge (SG)
147 Combined Precipitation Data Set was used during the study period. The data is available for
148 download from <https://measures.gesdisc.eosdis.nasa.gov/data/GPCP/GPCPMON.3.2/> (last
149 accessed June 5, 2025).

150 **Cloud-Aerosol LIDAR with Orthogonal Polarization (CALIOP)**

151 The CALIOP sensor on the Cloud-Aerosol Lidar and Infrared Pathfinder Satellite Observations
152 (CALIPSO) satellite provides data on atmospheric aerosols, including aerosol layer heights and
153 thicknesses, optical depth, aerosol type, and other optical properties (Omar et al., 2009; Kim et al.,
154 2018). In our study, we used vertical aerosol-type images available on the CALIPSO website.

155 **2..1.2 Reanalysis/model products**

156 **MERRA-2 reanalysis**

157 We used monthly mean geopotential height, wind vectors (zonal and meridional wind speeds),
158 and, total column black carbon, organic carbon, and particulate matter from the Modern-Era
159 Retrospective Analysis for Research and Applications, version 2 (MERRA-2). MERRA-2 is the
160 latest atmospheric reanalysis data produced by the NASA Global Modeling and Assimilation

161 Office (GMAO; Gelaro et al., 2017). The horizontal resolution of the MERRA-2 reanalysis is 0.5°
162 $\times 0.625^\circ$.

163 **Global Land Data Assimilation System (GLDAS)**

164 Monthly mean soil moisture content (10 - 40 cm underground) from the Global Land Data
165 Assimilation System (GLDAS)_NOAH025_M v2.1 is utilized. The data can be downloaded from
166 https://hydro1.gesdisc.eosdis.nasa.gov/data/GLDAS/GLDAS_NOAH025_M.2.1/ (last accessed:
167 June 05, 2025).

168 **2.1.3 Ground-based observations**

169 **AERONET**

170 In this study, we use the latest version (V3) of Level 2.0 AERONET data from two stations:
171 Dongsha Island (also called the Pratas Islands; Dongsha_Island, 20.70°N , 116.73°E , 5 m above
172 sea level) and Lulin Atmospheric Background Station (LABS, $23^\circ28'\text{N}$, $120^\circ52'\text{E}$, 2,862 m; Sheu
173 et al., 2010). These offer cloud-screened, quality-checked direct-sun AOD retrievals with
174 uncertainties of about ± 0.01 in the visible and ± 0.02 in the ultraviolet range (Giles et al., 2019;
175 Sinyuk et al., 2020).

176 The summary of the major data used in the present study is presented in **Table 1**.

177 **Table 1.** Details of various data products used in the present study.

| Data | Resolution | Source |
|-----------------------------|--------------------------|--------------------------------|
| Aerosol Optical Depth (AOD) | $1^\circ \times 1^\circ$ | Aqua and Terra satellite/MODIS |
| Carbon Monoxide (CO) | $1^\circ \times 1^\circ$ | MOPITT and AIRS |
| Burned Area (BA) | 500 m | Aqua and Terra satellite/MODIS |

| | | |
|--|--------------------------------|--|
| MODIS Collection 6.1 Fire Anomalies | | combined Terra and Aqua satellite/MODIS |
| Wind and Geopotential Height | $0.5^\circ \times 0.625^\circ$ | MERRA reanalysis |

178

179 **2.2 Methodology**

180 The anomalies in the various parameters for April 2023 were estimated by subtracting the April
181 background long-term mea (2003-2022) from April 2023 value.

182 The magnitude of the AOD/CO enhancement in April 2023 above the long-term background was
183 determined by comparing the average of April 2003-2022. We obtained the percentage change in
184 AOD/CO relative to the respective background using Equation 1:

185
$$\text{Relative change in percentage} = \left(\frac{x_i - \bar{x}}{\bar{x}} \right) \times 100 \quad (\text{Eq. 1})$$

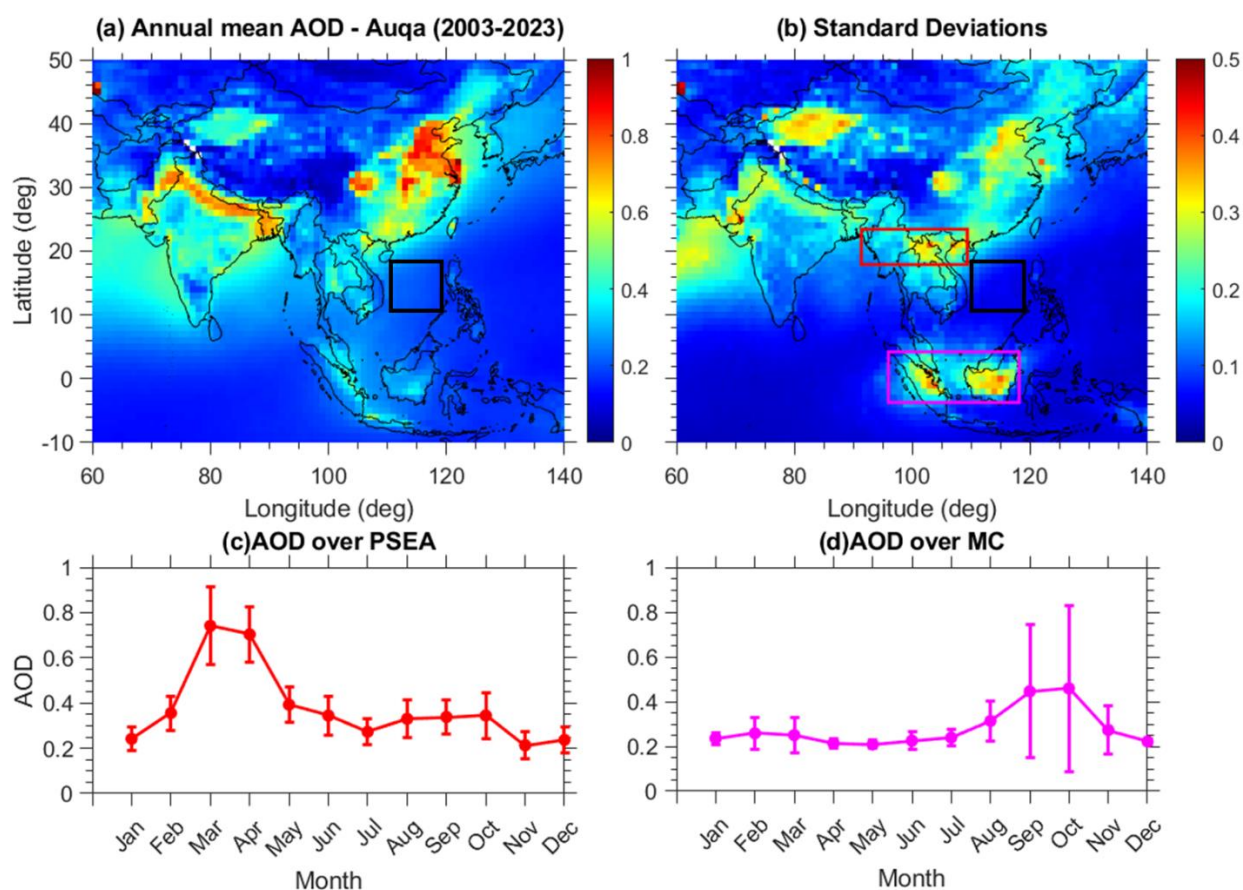
186 where x_i represents the monthly mean of April in 2023, and \bar{x} is the long-term mean of April
187 calculated using the data from 2003 to 2022.

188 **3. Results and Discussion**

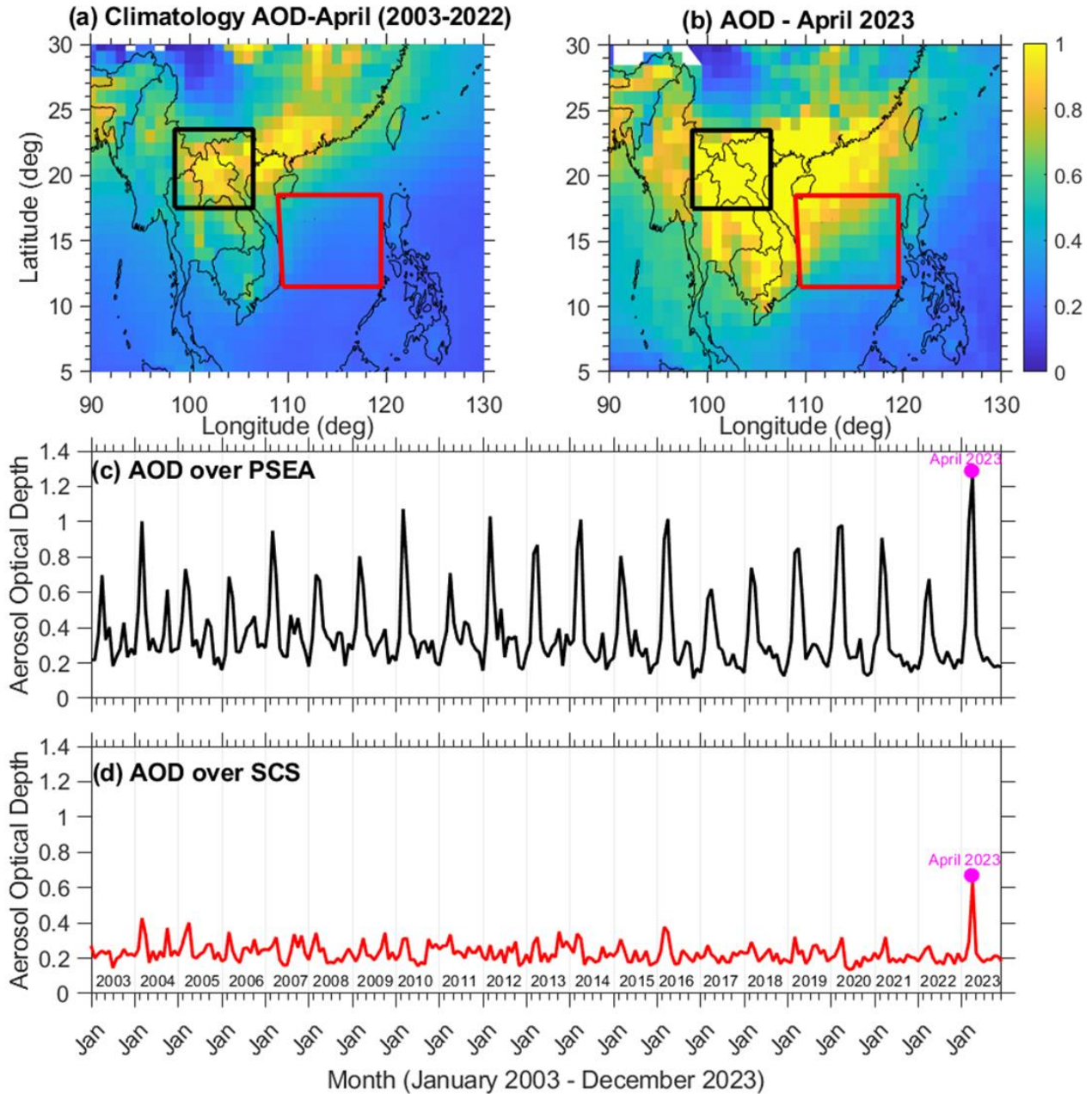
189 **3.1 Record-breaking aerosol loading over SCS in April 2023**

190 Aerosol optical depth (AOD) is a common metric for measuring atmospheric aerosol loading and
191 is crucial for radiative forcing assessments (Hirsch and Koren, 2021). In this study, we utilize AOD
192 data retrieved from the MODIS instruments aboard the Aqua and Terra satellites for the period
193 from 2003 to 2023. Before analyzing the unusual AOD conditions observed in April 2023, we first
194 characterize the long-term AOD behavior over the study area using two decades of MODIS data.
195 The spatial patterns of the long-term annual mean AOD and its associated standard deviation
196 across the Asian region are shown in **Figures 2a** and **2b**, respectively. Additionally, the long-term
197 monthly-mean variability of AOD over the two main biomass-burning (BB) regions surrounding
198 the SCS, namely PSEA and the MC, is shown in **Figures 2c** and **2d**. The relatively low AOD
199 levels and small standard deviations over the SCS suggest the dominance of a relatively clean
200 marine environment. The seasonal cycle of AOD shows clear peaks linked to regional BB activities

201 (Figs. 2c and 2d). Over PSEA, AOD peaks during March–April, while over the MC, the peak
 202 occurs in September–October. These seasonal maxima align with well-known BB activity periods
 203 in these areas (Ravindra Babu and Lin, 2024; Chang et al., 2024). The fire season over the MC
 204 usually runs from August to October, whereas PSEA experiences intense BB activity from January
 205 to April, with a notable peak in March.



206
 207 **Figure 2.** Climatological mean distribution of MODIS (a) Aerosol Optical Depth (AOD) and (b)
 208 respective standard deviations. The black box illustrated in both figures emphasizes the specific
 209 area of the South China Sea (SCS) that is the primary focus of this research. (109-119E, 11-18N).
 210 The red and magenta boxes indicate the PSEA and MC, two significant biomass-burning regions
 211 near the SCS. The long-term average seasonal variation in AOD is illustrated over (c) PSEA and
 212 (d) MC.

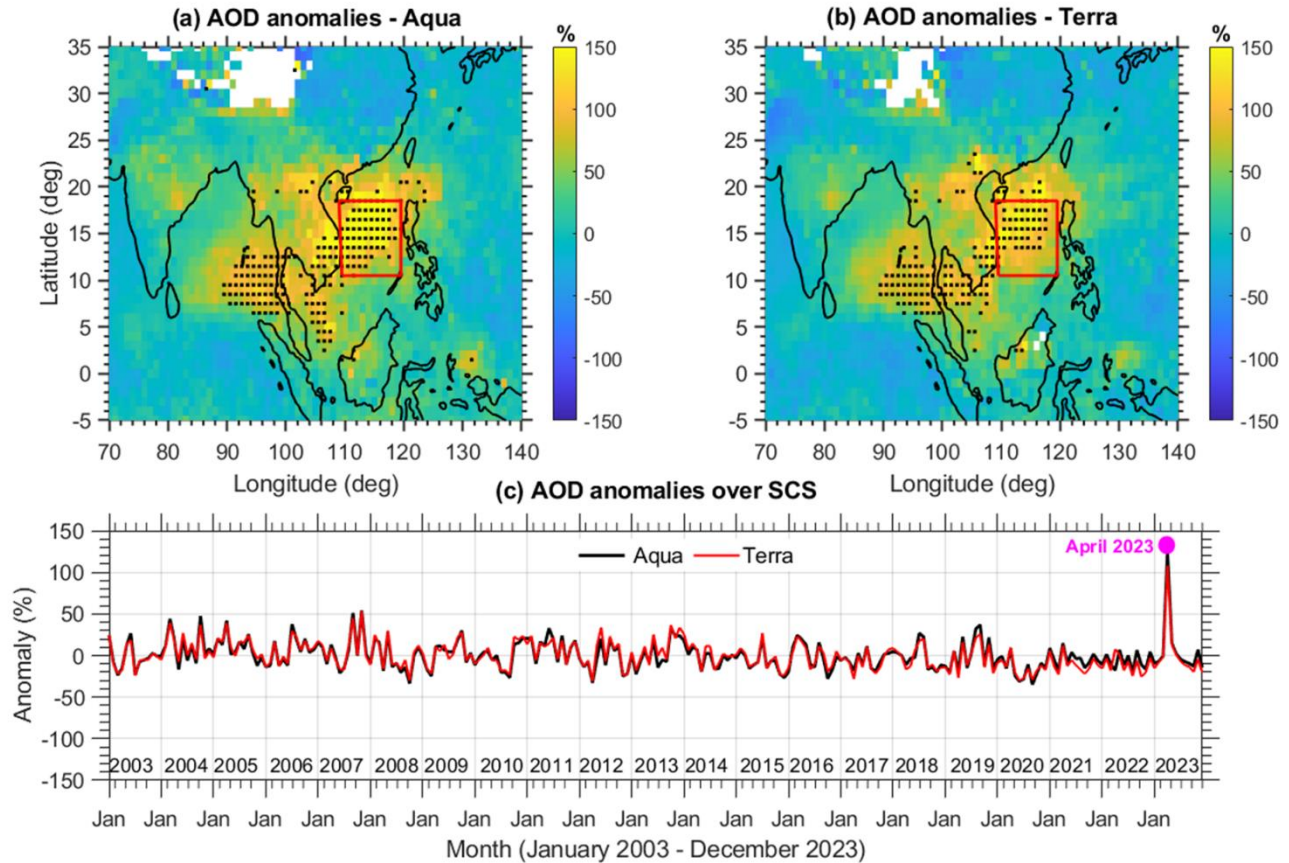


213

214 **Figure 3.** Spatial distribution of (a) Inter-annual (2003 to 2022) monthly average AOD values for
 215 April. (b) Monthly AOD values for April 2023. A notable increase in AOD values is observed
 216 over the peninsular Southeast Asia and the South China Sea. AOD distribution averaged in April
 217 over the past two decades showed a belt of high aerosol loading extending from northern Laos to
 218 the southern coast of China. During April 2023, extreme AOD values were observed across the
 219 entire PSEA, extending to coastal South China and the South China Sea. (c) Time series of average
 220 monthly mean AOD values over the northern Peninsula of Southeast Asia (17-23N, 99- 106E),
 221 and (d) over the South China Sea (109-119E, 11-18N) from January 2003 to December 2023. The
 222 magenta dot in subplots (c) and (d) marks the AOD values during April 2023.

223 To emphasize the anomalous conditions during April 2023, we present the spatial distribution of
224 April AOD over the study region for both the long-term average and April 2023 specifically. The
225 long-term average April AOD for 2003–2022 and the corresponding April 2023 AOD distribution
226 are shown in **Figures 3a** and **3b**. Moreover, the time series of monthly mean AOD from 2003 to
227 2023 over northern PSEA (17–23°N, 99–106°E) and the SCS (11–18°N, 109–119°E) are displayed
228 in **Figures 3c** and **3d**. The AOD distribution in April over two decades indicates high aerosol
229 loading from northern Laos to coastal South China (15–25 N, 100–120 E). In April 2023, extreme
230 AOD values extended from PSEA to South China and SCS, with the highest center between
231 northern Laos and the SCS. Record-breaking AOD levels were observed for the area averaged
232 over the SCS in April 2023, showing a nominal increase in northern PSEA (**Fig. 3c**). However,
233 the highest AOD value for northern PSEA in April 2023 correlates with record AOD over the SCS.
234 Long-term monthly mean AOD from Aqua and Terra (2003–2023) exhibited a strong correlation
235 of 0.97, confirming the consistency and reliability of these observations (**Fig. S1a** in the
236 Supplement). To assess the magnitude of the increase, we estimated the percentage change in AOD
237 by comparing April 2023 with the long-term average for April from 2003 to 2022.

238



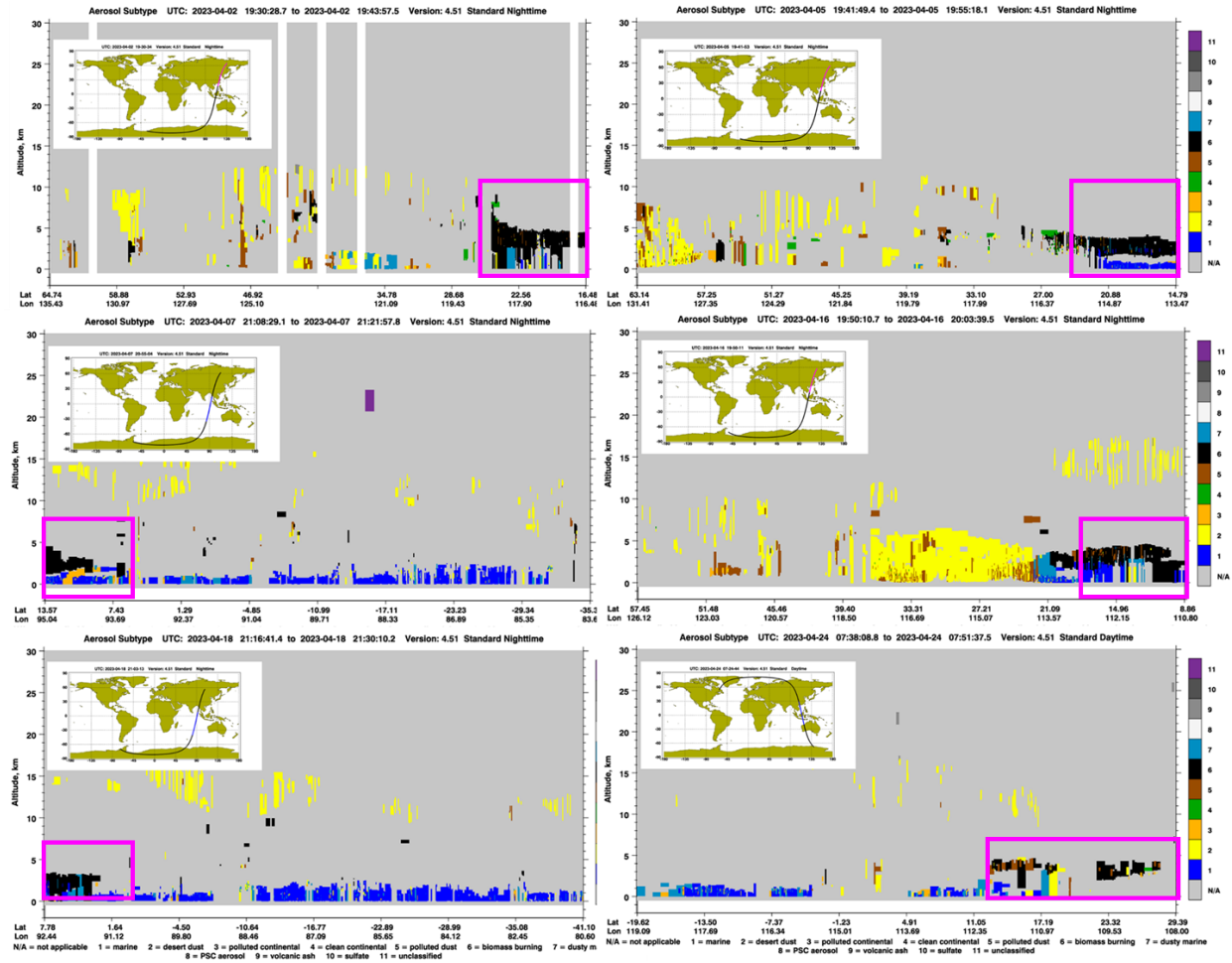
239

240 **Figure 4.** Spatial distribution of the change (%) in Aerosol Optical Depth (AOD) values during
 241 April 2023 compared with the inter-annual April average (2003-2022). (a) AOD anomalies are
 242 obtained from the MODIS Aqua and (b) from the MODIS Terra satellite. The black dots indicate
 243 that the anomalies exceed 4σ of the long-term mean. (c) Time series of area-averaged AOD
 244 anomalies expressed in percentage change over the South China Sea (SCS) domain from the Aqua
 245 (black line) and Terra (red line) satellites. The most pronounced enhancement occurred over the
 246 SCS, where April AOD anomalies exceeded 4σ above the long-term mean.

247 **Figures 4a** and **4b** depict the spatial extent of AOD anomalies expressed as percentage
 248 changes from MODIS Aqua and Terra. A surprising and widespread enhancement, with an
 249 increase of over 150% in most of the SCS and the southern Bay of Bengal (BoB), was evident in
 250 April 2023, and the increased anomalies exceeded approximately four standard deviation units.
 251 The area-averaged AOD anomalies (%) over the SCS domain from Aqua (black line) and Terra
 252 (red line) satellites show that the increase in April 2023 was a record high compared to MODIS
 253 data from 2003 to 2023, highlighting the extremity of AOD enhancement in that month. Satellite
 254 observations were further corroborated by ground-based in situ measurements from the
 255 AERONET. The only operational AERONET remote station downwind of PSEA biomass

256 burning, with over a decade of continuous AOD measurements (**Fig. S2a** in the Supplement),
257 within the SCS region is located on Dongsha Island (also known as Pratas Island, 20.70°N,
258 116.73°E; 5 m a.s.l.). Analysis of the monthly mean AOD data from Dongsha Island indicates that
259 April 2023 recorded the highest AOD value in the entire observational period from January 2009
260 to December 2023 (**Fig. S2c** in the Supplement). AERONET comparisons show strong
261 correlations with MODIS AOD: 0.86 for Aqua and 0.87 for Terra (Sup. Fig. 3), supporting the
262 reliability of the satellite observations. As AOD is a column-integrated measure, it does not
263 provide information on the vertical distribution of aerosols. To overcome this limitation, we further
264 analyzed vertical distribution images of aerosols from the Cloud-Aerosol Lidar and Infrared
265 Pathfinder Satellite Observation (CALIPSO), which reveal pronounced enhancements in smoke
266 aerosol over the SCS (**Fig. 5**). Elevated smoke layers were also observed over the southern BoB
267 in April 2023, predominantly within the mid-troposphere at altitudes of approximately 2–5 km.
268 Consistent with these lidar observations, MERRA-2 reanalysis data indicate substantial increases
269 in aerosol mass concentrations in 2023, with black carbon (BC) increasing by ~250% and organic
270 carbon (OC) by ~350% (**Fig. S4** in the Supplement). The most pronounced enhancements occur
271 between 700 and 600 hPa, closely matching the altitude range identified by CALIPSO. The
272 concurrence of satellite (MODIS and CALIPSO) and reanalysis data points to a severe pollution
273 episode in April 2023 over and surrounding regions of the SCS, characterized by elevated aerosol
274 layer indicative of long-range-transported biomass-burning smoke. Notably, the SCS is a relatively
275 clean remote marine region with limited local aerosol sources. In such environments, enhanced
276 aerosol loading is typically associated with long-range transport of pollutants from surrounding
277 continental regions (Pani, 2023). Given the potential influence of long-range pollution transport,
278 we further analyzed variations in carbon monoxide (CO), a widely used tracer of biomass-burning
279 emissions due to its relatively long atmospheric lifetime (~1–2 months) and strong association
280 with incomplete combustion (Ravindra Babu et al., 2023). We investigated CO changes across the
281 study region using measurements from the MOPITT and AIRS satellites, which together provide
282 more than two decades of continuous CO observations. CO data at 700 and 500 hPa from both
283 satellites were analyzed for the period 2003–2023, with the 500 hPa level representing the altitude
284 of maximum sensitivity for CO retrievals (Buchholz et al., 2021).

285

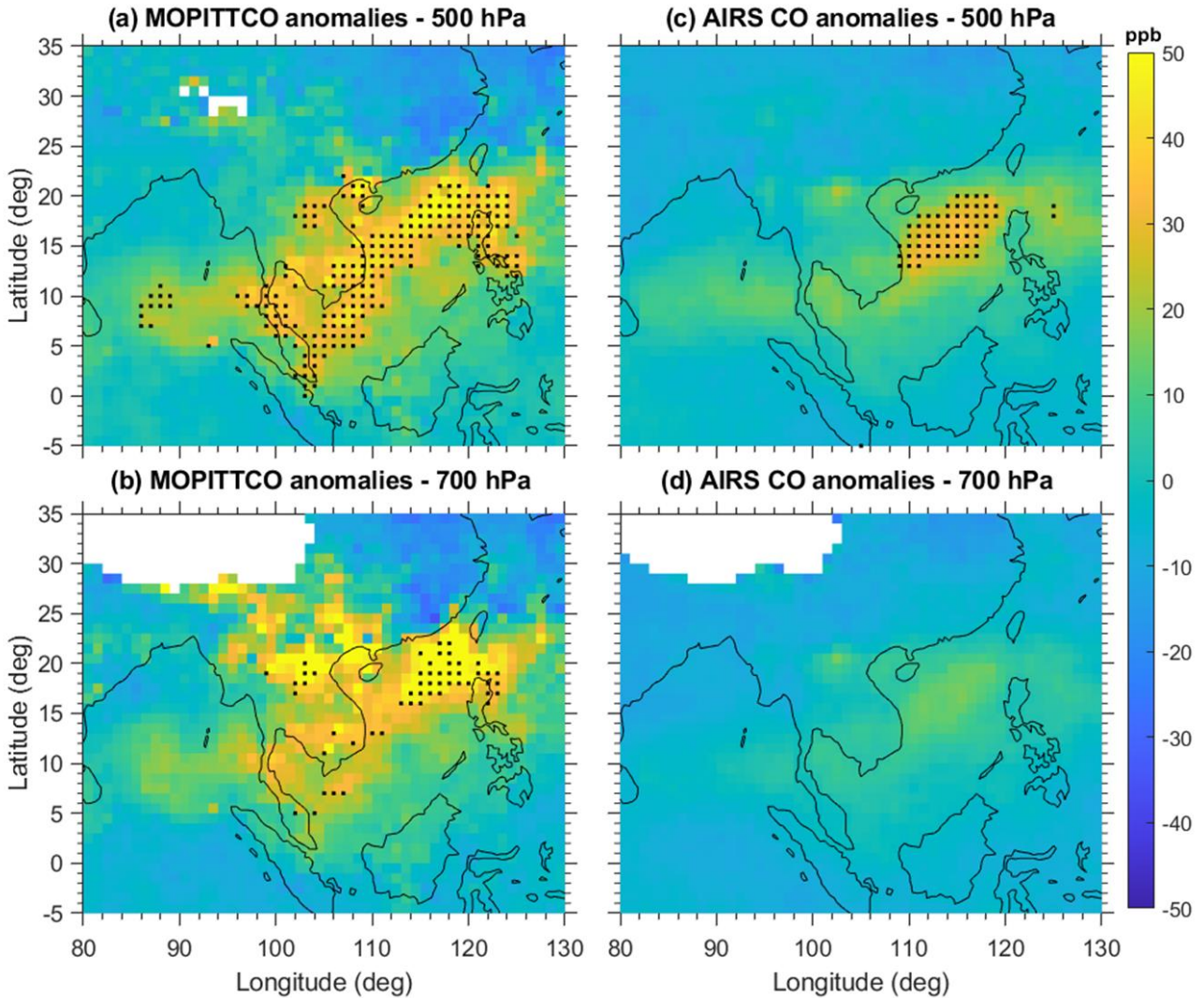


286

287 **Figure 5.** Aerosol subtype images obtained by the CALIPSO observations during various days in
 288 April 2023. The highlighted magenta box indicates elevated smoke over the SCS and the southern
 289 Bay of Bengal. Smoke aerosol is shown in black.

290 The observed CO anomalies from the two satellites are shown in **Fig. 6**, revealing
 291 significantly elevated CO concentrations over the SCS in April 2023, reaching up to 3σ above the
 292 2003–2022 climatology. Although MOPITT displays more spatially concentrated anomalies than
 293 AIRS, both datasets consistently show positive CO anomalies at both pressure levels, indicating a
 294 substantial increase in mid-tropospheric CO during this period. For MOPITT CO retrievals,
 295 primary sources of uncertainty include limitations in vertical sensitivity and potential retrieval
 296 biases (Sayer et al., 2014; Wei et al., 2019). However, the observed enhancements ($>3\sigma$) are
 297 supported by independent AIRS CO measurements, reinforcing the robustness of the detected
 298 anomalies. The comparison between MOPITT and AIRS CO at 500 hPa over the SCS further
 299 shows a strong positive correlation ($R \approx 0.89$; **Fig. S1b** in the Supplement). Furthermore, the

300 spatial distribution of CO anomalies closely resembles that of AOD anomalies (Fig. 4). Area-
301 averaged anomalies of AOD and 500 hPa CO over the SCS during 2003–2023 exhibit a strong
302 positive correlation ($R \approx 0.81$; **Fig. S5** in the Supplement), suggesting that long-range pollution
303 transport plays an important role in modulating April aerosol variability in this region. The bubble
304 chart further highlights the exceptional severity of the April 2023 event compared with previous
305 years (**Fig. S5** in the Supplement). Because CO is primarily produced through incomplete
306 combustion, elevated concentrations far from major traffic or industrial sources strongly suggest
307 biomass-burning and wildfire emissions. This indicates that smoke was likely transported from
308 surrounding regions toward the SCS and the BoB, which are located near major biomass-burning
309 hotspots, including the MC and PSEA. The MC fire season typically occurs from August to
310 October, whereas PSEA experiences a biomass-burning season from January to April, peaking in
311 March (**Fig. 2**). These seasonal characteristics strongly suggest that the elevated AOD levels
312 observed over the SCS in April 2023 were likely linked to biomass-burning activity in PSEA.
313 Overall, the April 2023 event is notable for its exceptional intensity and extensive spatial coverage.
314 The MODIS AOD anomalies were approximately four times higher than the long-term mean
315 across much of the SCS and the southern BoB during April 2023. We suggest that this episode
316 represents a rare, previously unreported extreme aerosol-loading event, distinct from the
317 springtime biomass-burning transport events over the PSEA region documented in earlier studies.
318 Such anomalously high aerosol loading over the SCS may have important implications for regional
319 air quality and climate, highlighting the need for further investigation into the underlying drivers
320 and physical mechanisms responsible for this event.



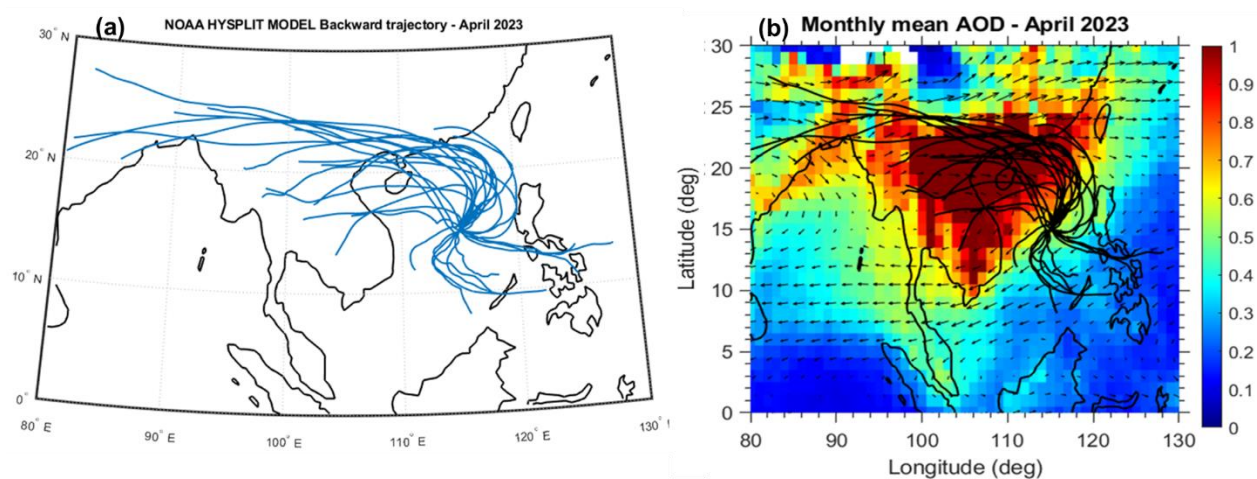
321

322 **Figure 6.** Spatial distribution of carbon monoxide (CO) anomalies in April 2023 at (a) 500 hPa
 323 and (b) 700 hPa from MOPITT satellite measurements. Panels (c) and (d) show the corresponding
 324 CO anomalies at 500 hPa and 700 hPa derived from AIRS satellite observations. Anomalies are
 325 calculated relative to the long-term April mean for 2003–2022. Black dots indicate regions where
 326 anomalies exceed the 3σ significance threshold.

327 **3.2 Transport and Source Attribution of the April 2023 Aerosol Event**

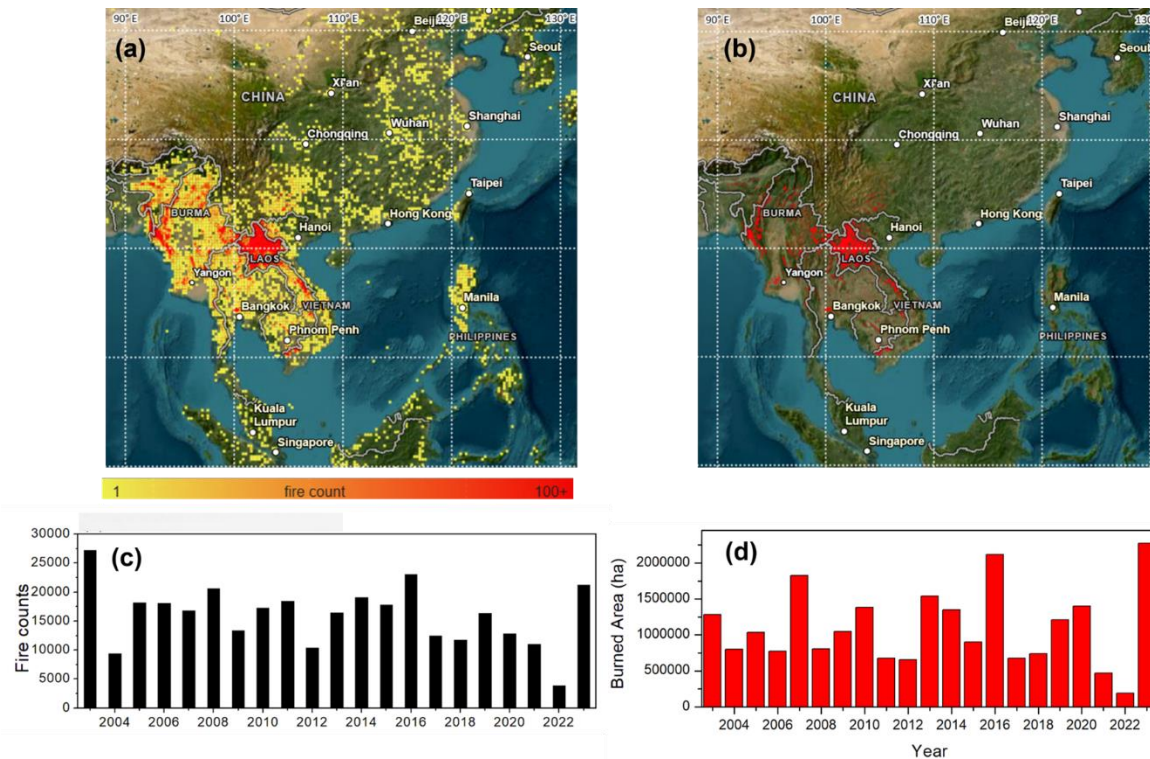
328 From the previous section, it is clear that most of the aerosols are free-troposphere-
 329 dominated and are located mostly in the $\sim 2\text{-}5\text{ km}$ region over SCS. To determine the source regions
 330 responsible for elevated aerosol concentrations over the SCS in April 2023, backward air-mass
 331 trajectories were computed using the HYSPLIT model. Trajectories were initialized at 15°N ,
 332 115°E , at 3 km above sea level, corresponding to the altitude range (2–5 km) of the elevated aerosol
 333 layer observed in CALIPSO and MERRA-2 profiles. Daily 72-hour trajectories (**Fig. 7a**) indicate

334 that air masses arriving over the SCS predominantly originated from northern PSEA. When
335 overlaid on the monthly mean MODIS AOD (**Fig. 7b**), these trajectories reveal transport pathways
336 that coincide with regions of high aerosol loading, confirming that long-range transport from
337 northern PSEA was the primary mechanism delivering BB emissions to the SCS. To see the BB
338 activity in April 2023, we used MODIS fire counts and Burned Area. The spatial distributions of
339 MODIS fire counts and burned area (BA) for April 2023 (**Figs. 8a–b**) show that BB activity was
340 overwhelmingly concentrated in northern PSEA, particularly in northern Laos and adjacent
341 regions of Myanmar and Thailand. Minimal fire activity and BA were observed over the MC and
342 southern China; these regions were therefore excluded from source-region calculations. Analysis
343 of inter-annual variability in April BB activity over PSEA from 2003 to 2023 (**Figs. 8c–d**),
344 considering only fire detections above the 80% confidence level, indicates substantial year-to-year
345 fluctuations. Notably, April 2023 recorded the highest burned area (~2.27 Mha) during the 21-year
346 period, highlighting the exceptional intensity of BB activity during this month.



347
348 **Figure 7.** (a) Daily 72-h NOAA HYSPLIT backward trajectories ending at 12:00 UTC at a
349 representative location (15°N, 115°E) over the South China Sea at 3 km altitude for April 2023.
350 (b) Same as (a), but overlaid on the monthly mean MODIS aerosol optical depth (AOD) for April
351 2023.

352



353

354 **Figure 8.** Spatial distribution of the (a) MODIS fire counts, (b) MODIS Global Burned Area
 355 Product in April 2023. Inter-annual variability in (c) Fire counts, and (d) Burned Area over
 356 Peninsula Southeast Asia in April from 2003 to 2023. (Source:
 357 <https://firms.modaps.eosdis.nasa.gov/>). For inter-annual variability in fire counts, we considered
 358 those above the 80% confidence level.

359 Country-level statistics (**Table 2**) further highlight the dominant contribution from Laos,
 360 which accounted for 11,877 fires (56.0%), 1.53×10^6 MW of fire radiative power (FRP; 63.5%),
 361 and 1.08×10^6 ha of burned area (47.7%). Notably, the BA observed in April 2023 represents the
 362 highest monthly value in the available dataset (2002–2023; **Fig. S6** in the Supplement).
 363 Approximately 60% of Laos is forested (**Fig. S7** in the Supplement), with much of this forest
 364 located in northern Laos where the majority of fires occurred during April 2023 (**Fig. 8a**).
 365 Myanmar contributed the second-largest share, with 7,054 fires (33.3%), 7.78×10^5 MW of FRP
 366 (32.3%), and 9.15×10^5 ha of burned area (40.3%). Thailand, Vietnam, and Cambodia contributed
 367 comparatively smaller burned areas of 1.21×10^5 ha, 1.30×10^5 ha, and 2.20×10^4 ha, respectively.
 368 In total, 21,198 fires across PSEA produced approximately 2.41×10^6 MW of FRP in April 2023.
 369 These results indicate that intense BB activity over northern PSEA, particularly northern Laos,
 370 was the primary source of the exceptional aerosol loading observed over the SCS in April 2023.
 371 However, two key questions remain: (i) what factors triggered the anomalously strong fire activity

372 in Laos during April 2023, and (ii) why were BB aerosols transported unusually far southward
 373 across the SCS and into the southern BoB, rather than following the more typical transport
 374 pathways toward Taiwan and the north western Pacific? To address these questions, we next
 375 examine the large-scale meteorological and dynamical circulation conditions prevailing during
 376 April 2023.

377 **Table 2.** MODIS total fire counts, the corresponding total accumulated fire radiative power (FRP),
 378 and the burned area (BA) observed over peninsular Southeast Asia (PSEA) and each country
 379 within PSEA in April 2023. The percentage contribution of each country to the total number of
 380 fires, the total FRP, and the BA of PSEA is shown in brackets.

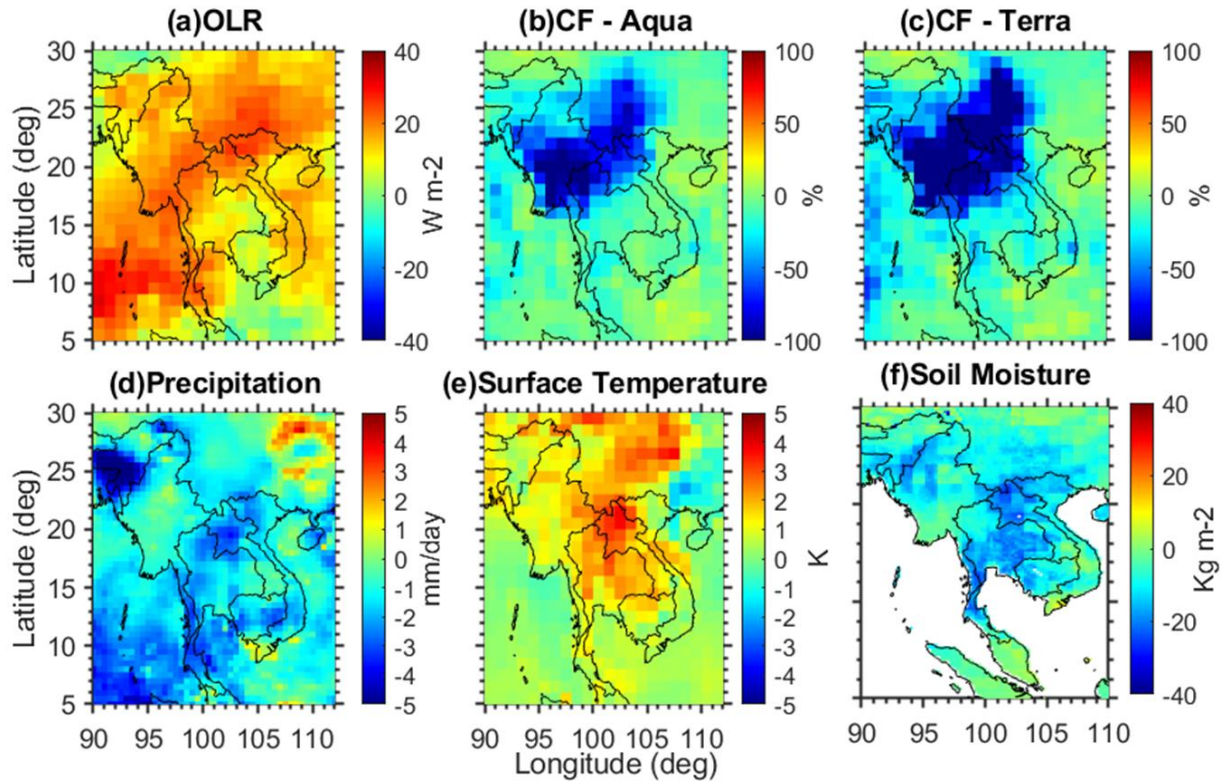
| Country | Total Fires | Fire Radiative Power (MW) | Burned Area (ha) |
|----------|----------------|---------------------------|-------------------|
| PSEA | 21198 | 2407283 | 2272099.89 |
| | | | |
| Country | Total Fires | FRP | BA |
| Cambodia | 242 (1.14%) | 13402 (0.5%) | 21959.5 (0.97%) |
| Laos | 11877 (56.02%) | 1530000 (63.5%) | 1084050 (47.71%) |
| Myanmar | 7054 (33.27%) | 777970 (32.32%) | 915175.7 (40.27%) |
| Thailand | 1322 (6.24%) | 50276 (2.1%) | 120573.7 (5.31%) |
| Vietnam | 703 (3.32%) | 35634 (1.5%) | 130340.7 (5.74%) |

381

382 **3.3 Large-scale meteorological and dynamical circulation anomalies in April 2023**

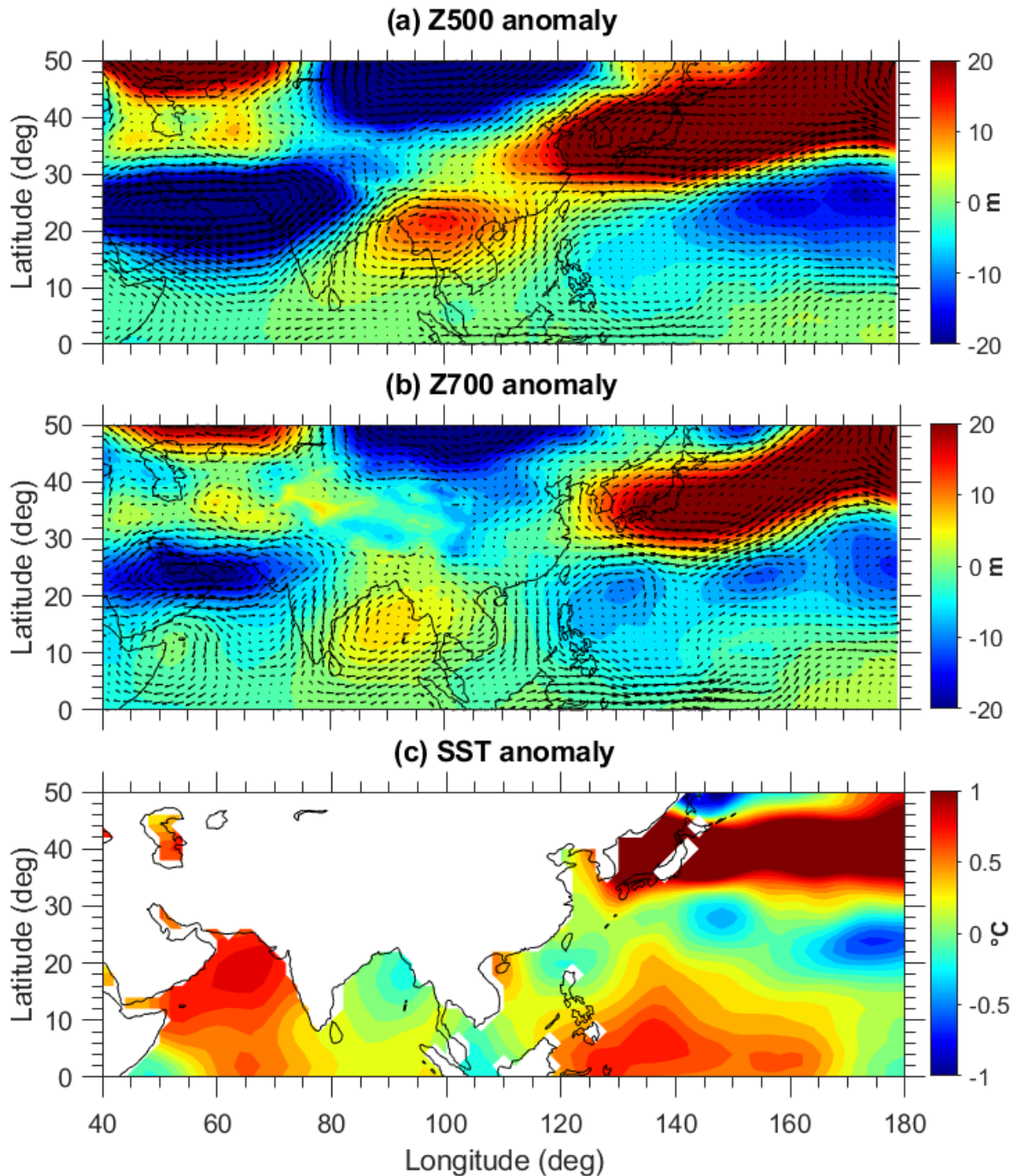
383 In this section, we examine the meteorological and large-scale dynamical circulation
 384 anomalies associated with the April 2023 event. **Figure 9** presents the spatial distribution of
 385 anomalies in key meteorological parameters during April 2023 relative to the 2003–2022
 386 climatological mean. As shown in **Figure 9**, anomalies in Outgoing Longwave Radiation (OLR)
 387 indicate suppressed convective activity over PSEA during April 2023. The reduced convection
 388 was accompanied by negative precipitation anomalies, elevated surface temperatures, and
 389 pronounced soil moisture (SM) deficits. These conditions are spatially consistent with the regions
 390 of enhanced fire counts and burned area observed by MODIS over northern Laos (**Fig. 8**). Long-

391 term SM anomalies over northern Laos reached exceptionally low values in April 2023,
392 representing the lowest levels in the past two decades (**Figs. S8a–b** in the Supplement). To further
393 examine the persistence of these conditions, we analyzed the temporal evolution of SM anomalies
394 during 2021–2023. The results show maximum positive anomalies in March 2022 and a transition
395 to strong negative anomalies by April 2023, indicating a prolonged drought from winter 2022 to
396 April 2023 (**Fig. S8c** in the Supplement). We further assessed the relationship between SM
397 anomalies and fire activity over Laos. The standardized fire anomalies and SM anomalies (**Fig. S9**
398 in the Supplement) reveal a significant inverse relationship: reduced SM is associated with
399 enhanced fire activity. In April 2023, extreme negative SM anomalies coincided with strong
400 positive fire anomalies, highlighting the role of severe surface drying in promoting intense
401 biomass-burning activity. A similar co-occurrence of anomalously low SM and elevated fire
402 activity is also evident in 2016, a year previously identified as having intensified regional burning.
403 These findings provide additional observational evidence that soil moisture deficits are linked to
404 enhanced fire activity over PSEA. Previous studies have shown that negative SM anomalies can
405 promote positive geopotential height anomalies in the upper troposphere, which tend to reinforce
406 local high-pressure conditions and enhance surface warming (e.g., Fischer et al., 2007; Dong et
407 al., 2023). Motivated by this mechanism, we next examine the large-scale dynamical circulation
408 patterns during April 2023 to understand how atmospheric dynamics may have contributed to the
409 observed meteorological anomalies and the anomalous transport of biomass-burning aerosols.



410

411 **Figure 9.** Surface and atmosphere conditions in April 2023. April anomalies in 2023 compared to
 412 the 2003-2022 climatological period for (a) Outgoing Longwave radiation (OLR), (b) cloud
 413 fraction (CF) from Aqua, (c) cloud fraction from Terra, (d) precipitation, (e) Surface Temperature,
 414 (f) soil moisture (10 - 40 cm underground). OLR and surface temperatures are obtained from AIRS
 415 satellite measurements. CF data from MODIS Aqua and Terra. Soil moisture is obtained from the
 416 GLDAS Noah Land Surface Model L4 monthly 0.25 x 0.25 degree V2.1. Precipitation data is
 417 obtained from the Global Precipitation Climatology Project (GPCP) Version 3.2.



418

419 **Figure 10.** Spatial distribution of (a) 500 hPa geopotential height (Z500), (b) 700 hPa geopotential
 420 height (Z700), and (c) Sea Surface Temperature (SST) anomalies in April 2023. The anomalies
 421 are calculated by subtracting the April 2023 monthly mean from the April climatology for the
 422 period 1991 to 2020. The wind anomalies for the respective pressure levels are overlaid in Z500
 423 and Z700 anomalies. The geopotential height and wind data are from the MERRA-2 reanalysis,
 424 while SST data are from the NOAA Extended Reconstructed SST V5.

425

426 Our analysis focuses on geopotential height and horizontal wind fields at the 700- and 500-
427 hPa levels. The geopotential height fields (Z700 and Z500) in April 2023 show clear departures
428 from the April climatology (1991–2020) (**Figs. S10–11** in the Supplement). At 700 hPa, the
429 climatological high-pressure system over the Indian region extended eastward toward PSEA, while
430 at 500 hPa the western Pacific subtropical anticyclone shifted westward to lie directly over PSEA.
431 Geopotential height anomalies relative to the 1991–2020 mean (**Fig. 10a–b**) reveal a pronounced
432 anti-cyclonic circulation centered over northern PSEA (~20°N, 100°E). Cyclonic anomalies over
433 the WNP near the Philippines and upstream over the Indian Ocean form a zonal low–high–low
434 (L–H–L) structure, consistent with a propagating Rossby wave train (Hu et al., 2024). An
435 additional anti-cyclonic anomaly is present over the mid-latitude North Pacific. These circulation
436 anomalies suppressed convection over PSEA, consistent with positive OLR anomalies and reduced
437 precipitation (**Fig. 9**). Subsidence associated with the anti-cyclonic circulation promoted clear-sky
438 conditions (**Fig. 9**) and surface warming, which, together with severe soil moisture deficits, created
439 favorable conditions for intense biomass burning across northern Laos. The circulation pattern also
440 altered regional transport pathways. The combined influence of the WNP cyclone, the BoB
441 anticyclone at 700 hPa, and the PSEA anticyclone at 500 hPa modified the background flow over
442 Southeast Asia. Meridional wind anomalies (**Figs. S12b–c** in the Supplement) show persistent
443 northerly flow over the SCS, enabling southward transport of smoke from northern PSEA toward
444 the SCS and further into the southern BoB. This pathway contrasts with the climatological
445 transport route that typically advects smoke toward Taiwan and the northwestern Pacific. Zonal
446 wind anomalies further indicate weakened mid-latitude westerlies and locally reversed easterlies
447 near Japan associated with a strong anti-cyclonic anomaly (**Figs. S12a–b** in the Supplement),
448 suppressing the typical eastward export of smoke. Consistent with this, AOD observations from
449 the high-altitude mountain Lulin Atmospheric Background Station obtained through AERONET
450 show no notable enhancement in April 2023 (**Fig. S13a** in the Supplement), indicating reduced
451 smoke transport toward the northwestern Pacific. AERONET comparisons show strong
452 correlations with MODIS AOD: 0.83 for Aqua and 0.84 for Terra (**Fig. S14** in the Supplement),
453 further supporting the reliability of the satellite observations as shown in the Dongsha data.
454 Overall, the anomalous circulation pattern, characterized by a BoB anticyclone and a WNP
455 cyclone, redirected biomass-burning plumes from northern PSEA toward the SCS and southern
456 BoB, producing the exceptional aerosol loading observed in April 2023.

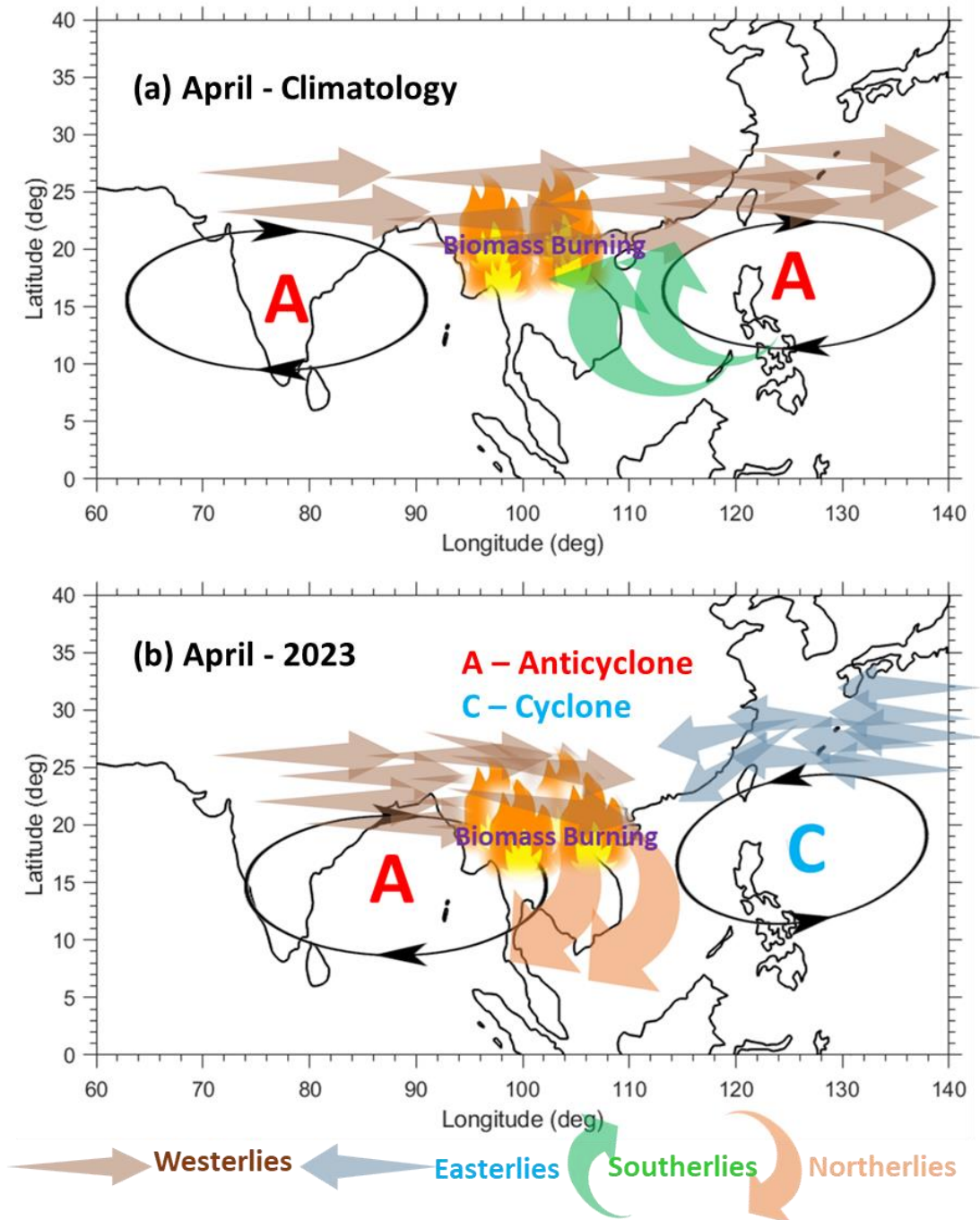
457 A key question is whether 2023 represents an exceptional biomass-burning (BB) year
458 relative to PSEA, or if similar conditions have occurred in other high-BB years. High-BB years
459 were identified using standardized fire anomalies from MODIS fire counts, with years exceeding
460 0.5 classified as high-BB (**Fig. S9** in the Supplement). Composites of MODIS AOD, 500-hPa
461 geopotential height, and wind vectors were constructed to represent typical circulation and aerosol
462 patterns during high-BB periods. Comparison with April 2023 shows notable differences: 2023
463 featured a stronger, more spatially coherent anti-cyclonic high over PSEA and substantially higher
464 AOD, indicating unusually intense aerosol loading. This suggests that circulation anomalies in
465 2023 amplified aerosol accumulation and transport beyond typical high-BB conditions (**Fig. S15**
466 in the Supplement). Another question is whether inter-annual variability associated with climate
467 oscillations, such as the El Niño–Southern Oscillation (ENSO), influenced BB activity and
468 circulation in 2023. SST anomalies linked to ENSO strongly modulate Indo-Pacific circulation
469 and hydro climate, with El Niño events typically enhancing springtime fires via drought, reduced
470 precipitation, and suppressed moisture transport (Yin, 2020; Zhu et al., 2021; Zheng et al., 2023).
471 We constructed composites of MODIS AOD and 500-hPa wind vectors for El Niño–ensuing and
472 La Niña–ensuing Aprils during 2003–2022 (**Fig. S16** in the Supplement). The results reveal higher
473 AOD over northern PSEA and coastal South China during El Niño-ensuing Aprils, accompanied
474 by a stronger anti-cyclonic system over PSEA extending from the BoB, consistent with enhanced
475 aerosol accumulation. In contrast, La Niña-ensuing Aprils show weaker circulation and lower
476 AOD. April 2023 occurred during the transition from a triple-dip La Niña to a developing El Niño,
477 deviating from typical ENSO-fire patterns. The anomalous anti-cyclonic and cyclonic circulations
478 over the BoB and western North Pacific in April 2023 are notable (**Fig. 10**), though their detailed
479 dynamics are beyond the scope of this study. Preliminary analysis revealed that SST warming over
480 the western Pacific warm pool and mid-latitude North Pacific, together with cooling over the
481 central-eastern equatorial Pacific, likely induced a Matsuno-Gill-type response, while warming in
482 the Arabian Sea and cooling in the BoB aligned with geopotential height anomalies, promoting
483 drought, intensified BB, and southward smoke transport toward the SCS and southern BoB (**Fig.**
484 **10c**; Gill, 1980; Zeng and Sun, 2022). Overall, the extreme aerosol event in April 2023 was shaped
485 not only by intense biomass burning but also by anomalous large-scale circulation linked to ocean–
486 atmosphere variability, highlighting the combined role of local and climate-scale drivers in
487 exceptional smoke events.

488 4. Summary and Conclusions

489 In April 2023, we observed an unprecedented increase in aerosol loading over the South
490 China Sea (SCS), which had not been recorded during the two-decade MODIS satellite
491 measurements period from 2003 to 2023. Satellite observations revealed ~150% increase in AOD
492 (MODIS), approximately four times higher than the long-term mean, alongside significant
493 enhancements in CO (MOPITT and AIRS) at the 700 and 500 hPa levels. This study investigates
494 the causes, physical mechanisms, and atmospheric dynamics underlying this extraordinary aerosol
495 event. Analyses of satellite data (MODIS, MOPITT, AIRS, and CALIPSO), NOAA HYSPLIT
496 back trajectories, and MERRA-2 reanalysis products indicate that intense biomass-burning activity
497 over northern Peninsular Southeast Asia was the primary driver of the record-breaking aerosol
498 loading over the SCS in April 2023. Our results further reveal that this BB activity was amplified
499 by exceptional meteorological conditions associated with unusually large-scale dynamical
500 circulation patterns. A dominant anti-cyclonic anomaly over PSEA suppressed convection, leading
501 to subsidence, elevated surface temperatures, and drought conditions that fueled fires, particularly
502 in Laos and Myanmar, which contributed most to the regional BB emissions. A schematic
503 summarizing these drivers and mechanisms is presented in **Figure 11**.

504 Climatologically, two anti-cyclones are typically situated over the WNP and the Indian
505 Ocean, producing predominantly southwesterly and southerly winds over the SCS. These southerly
506 winds generally transport BB smoke from PSEA to downwind regions such as Taiwan and the
507 WNP. In April 2023, however, the WNP anticyclone transformed into a cyclone, while the Indian
508 Ocean anticyclone shifted eastward over the BoB near PSEA. The resulting northerly flow over
509 the SCS, combined with easterly anomalies near Taiwan, blocked transport toward the
510 northwestern Pacific and redirected smoke from PSEA to the SCS and BoB. This circulation shift,
511 driven by the combined WNP cyclone and BoB anticyclone, highlights the critical role of large-
512 scale atmospheric dynamics in determining BB smoke pathways. These findings improve
513 understanding of transboundary pollution and can inform regional monitoring efforts over PSEA.

514



515

516 **Figure 11.** The schematic diagram illustrates the physical mechanisms responsible for the record-
 517 breaking aerosol loading over the South China Sea in April 2023.

518 The schematic illustrates the anomalous circulation and transport pathways responsible for the
 519 record aerosol loading over the South China Sea (SCS). A denotes the presence of an anticyclone
 520 anomaly, and C represents the presence of a cyclone anomaly. The horizontal arrows indicate
 521 subtropical free-tropospheric westerlies and easterlies. The green arrow indicates southerlies, and

522 northerlies are shown by the brown arrow, respectively. **Top panel:** climatological April (1991–
523 2020), showing the Bay of Bengal (BoB) and western Pacific anticyclones, southwesterly and
524 southerly winds over the SCS, and typical northward smoke transport toward Taiwan and the
525 western North Pacific. **Bottom panel:** April 2023 anomalies, with a pronounced PSEA
526 anticyclone, a western North Pacific cyclone, and an eastward-shifted BoB anticyclone. These
527 anomalies generate persistent northerlies over the SCS, suppress eastward transport, and redirect
528 biomass-burning plumes southward toward the SCS and southern BoB. Subsidence and reduced
529 convection over PSEA enhanced surface warming and drought, favoring intense fires.
530 Strengthened easterlies around Taiwan further inhibited northward export, producing the
531 exceptional aerosol accumulation observed in April 2023.

532 While the present study focuses on the record-breaking aerosol loading, its sources,
533 transport pathways, and dynamical drivers, the broader impacts of this extreme event remain
534 largely unexplored. In particular, aerosol-radiation interactions associated with such unusually
535 high AOD could substantially affect regional energy balance, atmospheric heating profiles, and
536 the hydrological cycle over adjacent regions. Future research will aim to quantify the radiative
537 forcing of these extreme aerosol concentrations and assess their broader atmospheric impacts.
538 Additionally, the exceptional increase in CO and other BB emissions may have strong implications
539 for tropospheric ozone formation, which will also be investigated. Interestingly, PSEA
540 experienced an extreme heatwave in April 2023, with record-high temperatures (Zachariah et al.,
541 2024; Lyu et al., 2024). Previous studies have attributed this heatwave to climate change
542 (Zachariah et al., 2024), as well as strengthened high-pressure systems, moisture deficits, and
543 strong land–atmosphere coupling (Lyu et al., 2024). Our results suggest a plausible contribution
544 from biomass-burning aerosols and associated greenhouse gases to this heatwave. Key questions
545 for future investigation include: How do greenhouse gases released by record-breaking BB activity
546 influence regional heat trapping? What is the impact of elevated aerosol concentrations on surface
547 radiation, cloud formation, and precipitation patterns? Addressing these questions will be critical
548 to understanding the exceptional conditions in PSEA and surrounding regions, including the
549 combined effects of BB aerosols and greenhouse gas emissions on regional climate extremes.

550
551
552
553

554 **Data availability**

555 MODIS data available from <https://modis.gsfc.nasa.gov/data/dataproduct/mod08.php>. The AIRS and
556 MOPITT CO data can be downloaded from https://disc.gsfc.nasa.gov/datasets/AIRS3STM_7.0
557 (AIRS project, 2019) and https://asdc.larc.nasa.gov/project/MOPITT/MOP02J_8 (NASA, 2023a).
558 MERRA-2 data are available online through the NASA Goddard Earth Sciences Data Information
559 Services Center (GES DISC; <https://disc.gsfc.nasa.gov>; NASA, 2023b). The MODIS fire and
560 burned area products can be downloaded from https://firms.modaps.eosdis.nasa.gov/active_fire/
561 (NASA, 2023c). Daily CALIPSO vertical distribution images of various aerosol types were
562 obtained from <https://www-calipso.larc.nasa.gov/products>. The NOAA HYSPLIT back
563 trajectories are retrieved from <https://www.ready.noaa.gov/HYSPLIT.php>. /

564 **Author Contributions**

565 **Saginela Ravindra Babu:** Conceptualization, Data curation, Formal analysis, Investigation,
566 Software, Validation, Visualization, Writing – original draft preparation, Writing – review and
567 editing; **Neng-Huei Lin:** Conceptualization, Investigation, Funding Acquisition, Supervision,
568 Resources, Writing – review and editing.

569 **Competing interests**

570 The authors declare no competing interests.

571 **Acknowledgements**

572 We acknowledge the National Science and Technology Council of Taiwan for supporting the
573 research. The authors thank NASA and NOAA for providing MOPITT, MODIS, CALIPSO and
574 AIRS satellite data. We thank NASA's Global Monitoring and Assimilation Office (GMAO) for
575 providing the Modern-Era Retrospective analysis for Research and Applications, Version 2
576 (MERRA-2) data.

577

578

579

580

581 **References**

582 Anderson, T. L., Charlson, R. J., Schwartz, S. E., Knutti, R., Boucher, O., Rodhe, H., and
583 Heintzenberg, J.: Climate forcing by aerosol– a hazy picture, *Science*, 300, 1103–1104,
584 <https://doi.org/10.1126/science.1084777>, 2003.

585 AIRS Project. Aqua/AIRS L3 Monthly Standard Physical Retrieval (AIRS-only) 1 degree x 1
586 degree V7.0 [Data set]. NASA Goddard Earth Sciences Data and Information Services Center.
587 <https://doi.org/10.5067/UBENJB9D3T2H>, 2020.

588 Buchholz, R. R., Worden, H. M., Park, M., Francis, G., Deeter, M. N., Edwards, D. P., Emmons,
589 L. K., Gaubert, B., Gille, J., Martinez-Alonso, S., Tang, W., Kumar, R., Drummond, J. R.,
590 Clerbaux, C., George, M., Coheur, P.-F., Hurtmans, D., Bowman, K. W., Luo, M., Payne, V. H.,
591 Worden, J. R., Chin, M., Levy, R. C., Warner, J., Wei, Z., and Kulawik, S. S.: Air pollution trends
592 measured from Terra: CO and AOD over industrial, fire-prone, and background regions, *Remote*
593 *Sens. Environ.*, 256, 112275, <https://doi.org/10.1016/j.rse.2020.112275>, 2021.

594 Byrne, B., Liu, J., and Bowman, K. W.: Carbon emissions from the 2023 Canadian wildfires,
595 *Nature*, 633, 835–839, <https://doi.org/10.1038/s41586-024-07878-z>, 2024.

596 Chan, C. Y., Chan, L. Y., Harris, J. M., Oltmans, S. J., Blake, D. R., Qin, Y., Zheng, Y. G., and
597 Zheng, X. D.: Characteristic of biomass burning emission sources, transport, and chemical
598 speciation in enhanced springtime tropospheric ozone profile over Hong Kong, *J. Geophys. Res.*,
599 108, 4015, <https://doi.org/10.1029/2001JD001555>, 2003.

600 Chang, J. H.-W., Wong, Y. J., Ooi, M. C.-G., Babu, S. R., Pani, S. K., and Lin, N.-H.: Biomass
601 burning in critical fire region over the Maritime Continent from 2012 to 2021: A review of the
602 meteorological influence and cloud-aerosol-radiation interactions, *Atmos. Environ.*, 320, 120324,
603 <https://doi.org/10.1016/j.atmosenv.2023.120324>, 2024.

604 Chuang, M.-T., Lee, C.-T., Chou, C. C.-K., Lin, N.-H., Sheu, G.-R., Wang, J.-L., Chang, S.-C., Wang,
605 S.-H., Chi, K. H., Young, C.-Y., Huang, H., Chen, H.-W., Weng, G.-H., Lai, S.-Y., Hsu, S.-P., Chang,
606 Y.-J., Chang, J.-H., and Wu, X.-C.: Carbonaceous aerosols in the air masses transported from
607 Indochina to Taiwan: Longterm observation at Mt. Lulin, *Atmos. Environ.*, 89, 507–516,
608 <https://doi.org/10.1016/j.atmosenv.2013.11.066>, 2014.

609 Cohen, J. B.: Quantifying the occurrence and magnitude of the Southeast Asian fire climatology,
610 *Environ. Res. Lett.*, 9, 114018, <https://doi.org/10.1088/1748-9326/9/11/114018>, 2014.

611 Cohen, J. B., Lecoecur, E., and Hui Loong Ng, D.: Decadal-scale relationship between
612 measurements of aerosols, land-use change, and fire over Southeast Asia, *Atmos. Chem. Phys.*,
613 17, 721–743, <https://doi.org/10.5194/acp-17-721-2017>, 2017.

614

615 Cordero, R. R., Feron, S., Damiani, A., Carrasco, J., Karas, C., Wang, C., Kraamwinkel, C. T., and
616 Beaulieu, A.: Extreme fire weather in Chile driven by climate change and El Niño–Southern
617 Oscillation (ENSO), *Sci. Rep.*, 14, 1974, <https://doi.org/10.1038/s41598-024-52481-x>, 2024.

618 Cui, D., Wang, J., Tan, L., and Dong, Z.: Impact of atmospheric wet deposition on phytoplankton
619 community structure in the South China Sea. *Estuar. Coast. Shelf Sci.* 173: 1–8,
620 <https://doi.org/10.1016/j.ecss.2016.02.011>, 2016.

621 Crutzen, P. J. and Andreae, M. O.: Biomass Burning in the Tropics: Impact on Atmospheric
622 Chemistry and Biogeochemical Cycles, *Science*, 250, 1669–1678,
623 <https://doi.org/10.1126/science.250.4988.1669>, 1990.

624 Deeter, M. N., Edwards, D. P., Francis, G. L., Gille, J. C., Mao, D., Martínez-Alonso, S., Worden,
625 H. M., Ziskin, D., and Andreae, M. O.: Radiance-based retrieval bias mitigation for the MOPITT
626 instrument: the version 8 product, *Atmos. Meas. Tech.*, 12, 4561–4580,
627 <https://doi.org/10.5194/amt-12-4561-2019>, 2019.

628 Dong, Z., Yang, R., Cao, J., Wang, L., and Cheng, J.: A strong high-temperature event in late-
629 spring 2023 in Yunnan province, Southwest China: Characteristics and possible causes. *Atmos.*
630 *Res.*, 295, 107017. <https://doi.org/10.1016/j.atmosres.2023.107017>, 2023.

631 Espinoza, J.-C., Jimenez, J. C., Marengo, J. A., Schongart, J., Ronchail, J., Lavado-Casimiro, W.,
632 and Ribeiro, J. V. M.: The new record of drought and warmth in the Amazon in 2023 related to
633 regional and global climatic features, *Sci. Rep.*, 14, 8107, [https://doi.org/10.1038/s41598-024-](https://doi.org/10.1038/s41598-024-58782-5)
634 [58782-5](https://doi.org/10.1038/s41598-024-58782-5), 2024.

635 Fischer, E. M., Seneviratne, S. I., Vidale, P. L., Lüthi, D., and Schär, C.: Soil Moisture –
636 Atmosphere Interactions during the 2003 European Summer Heat Wave, *J. Climate*, 20, 5081–
637 5099, <https://doi.org/10.1175/JCLI4288.1>, 2007.

638 Forster, P., Storelvmo, T., Armour, K., Collins, W., Dufresne, J.-L., Frame, D., Lunt, D. J.,
639 Mauritsen, T., Palmer, M. D., Watanabe, M., Wild, M., and Zhang, H.: The Earth's Energy Budget,
640 Climate Feedbacks, and Climate Sensitivity, in: *Climate Change 2021: The Physical Science*
641 *Basis, Contribution of Working Group I to the Sixth Assessment Report of the Intergovernmental*
642 *Panel on Climate Change*, edited by: Masson-Delmotte, V., Zhai, P., Pirani, A., Connors, S. L.,
643 Péan, C., Berger, S., Caud, N., Chen, Y., Goldfarb, L., Gomis, M. I., Huang, M., Leitzell, K.,
644 Lonnoy, E., Matthews, J. B. R., Maycock, T. K., Waterfield, T., Yelekçi, O., Yu, R., and Zhou,
645 B., Cambridge University Press, Cambridge, United Kingdom and New York, NY, USA, pp. 923–
646 1054, <https://doi.org/10.1017/9781009157896.009>, 2021.

647 Forster, P. M., Smith, C., Walsh, T., Lamb, W. F., Lamboll, R., Hall, B., Hauser, M., Ribes, A.,
648 Rosen, D., Gillett, N. P., Palmer, M. D., Rogelj, J., von Schuckmann, K., Trewin, B., Allen, M.,
649 Andrew, R., Betts, R. A., Borger, A., Boyer, T., Broersma, J. A., Buontempo, C., Burgess, S.,
650 Cagnazzo, C., Cheng, L., Friedlingstein, P., Gettelman, A., Gütschow, J., Ishii, M., Jenkins, S.,
651 Lan, X., Morice, C., Mühle, J., Kadow, C., Kennedy, J., Killick, R. E., Krummel, P. B., Minx, J.
652 C., Myhre, G., Naik, V., Peters, G. P., Pirani, A., Pongratz, J., Schleussner, C.-F., Seneviratne, S.

653 I., Szopa, S., Thorne, P., Kovilakam, M. V. M., Majamäki, E., Jalkanen, J.-P., van Marle, M.,
654 Hoesly, R. M., Rohde, R., Schumacher, D., van der Werf, G., Vose, R., Zickfeld, K., Zhang, X.,
655 Masson-Delmotte, V., and Zhai, P.: Indicators of Global Climate Change 2023: annual update of
656 key indicators of the state of the climate system and human influence, *Earth Syst. Sci. Data*, 16,
657 2625–2658, <https://doi.org/10.5194/essd-16-2625-2024>, 2024.

658 Gelaro, R., McCarty, W., Suarez, M. J., Todling, R., Molod, A., Takacs, L., Randles, C. A.,
659 Darmenov, A., Bosilovich, M. G., Reichle, R., Wargan, K., Coy, L., Cullather, R., Draper, C.,
660 Akella, S., Buchard, V., Conaty, A., da Silva, A. M., Gu, W., Kim, G.-K., Koster, R., Lucchesi,
661 R., Merkova, D., Nielsen, J. E., Partyka, G., Pawson, S., Putman, W., Rienecker, M., Schubert, S.
662 D., Sienkiewicz, M., and Zhao, B.: The Modern-Era Retrospective Analysis for Research and
663 Applications, Version 2 (MERRA-2), *J. Climate*, 30, 5419–5454, [https://doi.org/10.1175/JCLI-D-](https://doi.org/10.1175/JCLI-D-16-0758.1)
664 16-0758.1, 2017.

665 Giglio, L., Csiszar, I., and Justice, C. O.: Global distribution and seasonality of active fires as
666 observed with the Terra and Aqua Moderate Resolution Imaging Spectroradiometer (MODIS)
667 sensors, *J. Geophys. Res.-Biogeophys.*, 111, <https://doi.org/10.1029/2005JG000142>, 2006.

668 Giglio, L., Schroeder, W., and Justice, C. O.: The collection 6 MODIS active fire detection
669 algorithm and fire products, *Remote Sens. Environ.*, 178, 31–41,
670 <https://doi.org/10.1016/j.rse.2016.02.054>, 2016.

671 Giglio, L., Boschetti, L., Roy, D. P., Humber, M. L., and Justice, C. O.: The Collection 6 MODIS
672 burned area mapping algorithm and product, *Remote Sens. Environ.*, 217, 72–85,
673 <https://doi.org/10.1016/j.rse.2018.08.005>, 2018.

674 Gill, A. E.: Some simple solutions for heat-induced tropical circulation. *Q. J. R. Meteorol. Soc.*
675 106, 447–462. <https://doi.org/10.1002/qj.49710644905>, 1980.

676 Giles, D. M., Sinyuk, A., Sorokin, M. G., Schafer, J. S., Smirnov, A., Slutsker, I., Eck, T. F.,
677 Holben, B. N., Lewis, J. R., Campbell, J. R., Welton, E. J., Korkin, S. V., and Lyapustin, A. I.:
678 Advancements in the Aerosol Robotic Network (AERONET) Version 3 database– automated near-
679 real-time quality control algorithm with improved cloud screening for Sun photometer aerosol op
680 tical depth (AOD) measurements, *Atmos. Meas. Tech.*, 12, 169–209, [https://doi.org/10.5194/amt-](https://doi.org/10.5194/amt-12-169-2019)
681 12-169-2019, 2019.

682 Gui, Y., Wang, K., Jin, Z., Wang, H., Deng, H., Li, X., Tian, X., Wang, T., Chen, W., Wang, T.,
683 and Piao, S.: The decline in tropical land carbon sink drives high atmospheric CO₂ growth rate in
684 2023, *Natl. Sci. Rev.*, nwae365, <https://doi.org/10.1093/nsr/nwae365>, 2024.

685 Hirsch, E. and Koren, I.: Record-breaking aerosol levels explained by smoke injection into the
686 stratosphere, *Science*, 371, 1269–1274, <https://doi.org/10.1126/science.abe1415>, 2021.

687 Hu, Y., Yue, X., and Tian, C.: Climatic drivers of the Canadian wildfire episode in 2023,
688 *Atmospheric and Oceanic Science Letters*, 17, 100483,
689 <https://doi.org/10.1016/j.aosl.2024.100483>, 2024.

690 Huang, H.-Y., Wang, S.-H., Huang, W.-X., Lin, N.-H., Chuang, M.-T., da Silva, A. M., and Peng,
691 C.-M.: Influence of Synoptic-Dynamic Meteorology on the Long-Range Transport of Indochina
692 Biomass Burning Aerosols, *J. Geophys. Res.-Atmos.*, 125, e2019JD031260,
693 <https://doi.org/10.1029/2019JD031260>, 2020.

694 Huang, H.-Y., Wang, S.-H., Lau, W.K.M., Wang, S.-Y.S., and da Silva, A.M.: Impact of regional
695 climate patterns on the biomass burning emissions and transport over Peninsular Southeast Asia,
696 2000–2019. *Atmos. Res.* 297, 107067. <https://doi.org/10.1016/j.atmosres.2023.107067>, 2024.

697 IPCC: Climate Change 2021 – The Physical Science Basis: Working Group I Contribution to the
698 Sixth Assessment Report of the Intergovernmental Panel on Climate Change, Cambridge
699 University Press, Cambridge, <https://doi.org/10.1017/9781009157896>, 2023.

700 Jain, P., Barber, Q. E., Taylor, S. W., Whitman, E., Castellanos Acuna, D., Boulanger, Y.,
701 Chavardès, R. D., Chen, J., Englefield, P., Flannigan, M., Girardin, M. P., Hanes, C. C., Little, J.,
702 Morrison, K., Skakun, R. S., Thompson, D. K., Wang, X., and Parisien, M.-A.: Drivers and
703 impacts of the record-breaking 2023 wildfire season in Canada, *Nature Communications*, 15, 6764,
704 <https://doi.org/10.1038/s41467-024-51154-7>, 2024.

705 Jones, M. W., Kelley, D. I., Burton, C. A., Di Giuseppe, F., Barbosa, M. L. F., Brambleby, E.,
706 Hartley, A. J., Lombardi, A., Mataveli, G., McNorton, J. R., Spuler, F. R., Wessel, J. B.,
707 Abatzoglou, J. T., Anderson, L. O., Andela, N., Archibald, S., Armenteras, D., Burke, E.,
708 Carmenta, R., Chuvieco, E., Clarke, H., Doerr, S. H., Fernandes, P. M., Giglio, L., Hamilton, D.
709 S., Hantson, S., Harris, S., Jain, P., Kolden, C. A., Kurvits, T., Lampe, S., Meier, S., New, S.,
710 Parrington, M., Perron, M. M. G., Qu, Y., Ribeiro, N. S., Saharjo, B. H., San-Miguel-Ayanz, J.,
711 Shuman, J. K., Tanpipat, V., van der Werf, G. R., Veraverbeke, S., and Xanthopoulos, G.: State
712 of Wildfires 2023–2024, *Earth Syst. Sci. Data*, 16, 3601–3685, [https://doi.org/10.5194/essd-16-](https://doi.org/10.5194/essd-16-3601-2024)
713 3601-2024, 2024.

714 Ke, P., Ciais, P., Sitch, S., Li, W., Bastos, A., Liu, Z., Xu, Y., Gui, X., Bian, J., Goll, D. S., Xi, Y.,
715 Li, W., O'Sullivan, M., Goncalves De Souza, J., Friedlingstein, P., and Chevallier, F.: Low latency
716 carbon budget analysis reveals a large decline of the land carbon sink in 2023, *National Science*
717 *Review*, 11, nwae367, <https://doi.org/10.1093/nsr/nwae367>, 2024.

718 Kim, M.-H., Omar, A. H., Tackett, J. L., Vaughan, M. A., Winker, D. M., Treppe, C. R., Hu, Y.,
719 Liu, Z., Poole, L. R., Pitts, M. C., Kar, J., and Magill, B. E.: The CALIPSO version 4 automated
720 aerosol classification and lidar ratio selection algorithm, *Atmos. Meas. Tech.*, 11, 6107–6135,
721 <https://doi.org/10.5194/amt11-6107-2018>, 2018.

722 Kolden, C. A., Abatzoglou, J. T., Jones, M. W., and Jain, P.: Wildfires in 2023, *Nat. Rev. Earth*
723 *Environ.*, 5, 238–240, <https://doi.org/10.1038/s43017-024-00544-y>, 2024.

724 Lai, G. and Zhang Y.: Increased atmospheric aridity and reduced precipitation drive the 2023
725 extreme wildfire season in Canada. *Geophys. Res. Lett.*, 52, e2024GL114492.
726 <https://doi.org/10.1029/2024GL114492>, 2025.

- 727 Liao, Z. H., Ling, Z. H., Gao, M., Sun, J. R., Zhao, W., Ma, P. K., Quan, J. N., and Fan, S. J.:
728 Tropospheric Ozone Variability Over Hong Kong Based on Recent 20 years (2000–2019)
729 Ozonesonde Observation, *J. Geophys. Res.-Atmos.*, 126, <https://doi.org/10.1029/2020jd033054>,
730 2021.
- 731 Lemus-Canovas, M., Insua-Costa, D., Trigo, R. M., and Miralles, D. G.: Record-shattering 2023
732 Spring heatwave in western Mediterranean amplified by long-term drought, *npj Climate and*
733 *Atmospheric Science*, 7, 25, <https://doi.org/10.1038/s41612-024-00569-6>, 2024.
- 734 Lee, C.-T., Ram, S. S., Nguyen, D. L., Chou, C. C., Chang, S.-Y., Lin, N.-H., Chang, S.-C., Hsiao,
735 T.-C., Sheu, G.-R., and Ou-Yang, C.-F.: Aerosol chemical profile of near-source biomass burning
736 smoke in Sonla, Vietnam during 7-SEAS campaigns in 2012 and 2013, *Aerosol Air Qual. Res.*,
737 16, 2603–2617, 2016.
- 738 Lin, N.-H., Tsay, S.-C., Maring, H. B., Yen, M.-C., Sheu, G.-R., Wang, S.-H., Chi, K. H., Chuang,
739 M.-T., Ou-Yang, C.-F., Fu, J. S., Reid, J. S., Lee, C.-T., Wang, L.-C., Wang, J.-L., Hsu, C. N.,
740 Sayer, A. M., Holben, B. N., Chu, Y.-C., Nguyen, X. A., Sopajaree, K., Chen, S.-J., Cheng, M.-
741 T., Tsuang, B.-J., Tsai, C.-J., Peng, C.-M., Schnell, R. C., Conway, T., Chang, C.-T., Lin, K.-S.,
742 Tsai, Y. I., Lee, W.-J., Chang, S.-C., Liu, J.-J., Chiang, W.-L., Huang, S.-J., Lin, T.-H., and Liu,
743 G.-R.: An overview of regional experiments on biomass burning aerosols and related pollutants in
744 Southeast Asia: From BASE-ASIA and the Dongsha Experiment to 7-SEAS, *Atmos. Environ.*, 78,
745 1–19, <https://doi.org/10.1016/j.atmosenv.2013.04.066>, 2013.
- 746 Lin, C.-Y., Hsu, H.-M., Lee, Y. H., Kuo, C. H., Sheng, Y.-F., and Chu, D. A.: A new transport
747 mechanism of biomass burning from Indochina as identified by modeling studies, *Atmos. Chem.*
748 *Phys.*, 9, 7901–7911, <https://doi.org/10.5194/acp-9-7901-2009>, 2009.
- 749 Lin, C. C., Chen, W. N., Loftus, A. M., Lin, C. Y., Fu, Y. T., Peng, C. M., and Yen, M. C.:
750 Influences of the long-range transport of biomass-burning pollutants on surface air quality during
751 7-SEAS field campaigns, *Aerosol Air Qual. Res.*, 17, 2595–2607,
752 <https://doi.org/10.4209/aaqr.2017.08.0273>, 2017.
- 753 Li, J. Li X. and Ying T.: North Atlantic and the Barents Sea variability contribute to the 2023
754 extreme fire season in Canada. *Proc. Natl Acad. Sci. USA*, 121 (49).
755 <https://doi.org/10.1073/pnas.241424112>, 2024.
- 756 Liu, H., Jacob, D. J., Chan, L. Y., Oltmans, S. J., Bey, I., Yantosca, R. M., Harris, J. M., Duncan,
757 B. N., and Martin, R. V.: Sources of tropospheric ozone along the Asian Pacific Rim: An analysis
758 of ozonesonde observations, *J. Geophys. Res.*, 107, ACH 3-1-ACH 3-19,
759 <https://doi.org/10.1029/2001JD002005>, 2002.
- 760 Liu, Z., Deng, Z., Davis, S. J., and Ciais, P.: Global carbon emissions in 2023, *Nature Reviews*
761 *Earth and Environment*, 1–2, <https://doi.org/10.1038/s43017-024-00532-2>, 2024.
- 762 Lyu, Y., Wang, J., Zhi, X., Wang, X., Zhang, H., Wen, Y., Park, E., Lee, J., Wan, X., Zhu, S.,
763 Dung, D.T.: The characterization, mechanism, predictability, and impacts of the unprecedented

- 764 2023 Southeast Asia heatwave. *npj Clim. Atmos. Sci.* 7, 246. [https://doi.org/10.1038/s41612-024-](https://doi.org/10.1038/s41612-024-00797-w)
765 00797-w, 2024.
- 766 Ma, T., Chen, W., Cai, Q., Dong, Z., Wang, L., Hu, P., Gao, L., Garfinkel, C.: Attribution analysis
767 of the persistent and extreme drought in Southwest China during 2022–2023. *Environ. Res. Lett.*
768 <https://doi.org/10.1088/1748-9326/ad8171>, 2024.
- 769 MacCarthy, J., Tyukavina, A., Weisse, M.J., Harris, N., & Glen, E., Extreme wildfires in Canada
770 and their contribution to global loss in tree cover and carbon emissions in 2023. *Global Change*
771 *Biology*, 30, e17392. doi:10.1111/gcb.17392, 2024.
- 772 McMillan, W. W., Barnet, C., Strow, L., Chahine, M. T., McCourt, M. L., Warner, J. X., Novelli,
773 P. C., Korontzi, S., Maddy, E. S., and Datta, S.: Daily global maps of carbon monoxide from
774 NASA's Atmospheric Infrared Sounder, *Geophys. Res. Lett.*, 32, L11801,
775 <https://doi.org/10.1029/2004GL021821>, 2005.
- 776 McMillan, W. W., Evans, K. D., Barnet, C. D., Maddy, E. S., Sachse, G. W., and Diskin, G. S.:
777 Validating the AIRS Version 5 CO retrieval with DACOM in situ measurements during INTEX-
778 A and -B, *IEEE T. Geosci. Remote*, 49, 2802–2813, <https://doi.org/10.1109/TGRS.2011.2106505>,
779 2011.
- 780 Michailidis, K., Garane, K., Karagkiozidis, D., Peletidou, G., Voudouri, K.-A., Balis, D., and Bais,
781 A.: Extreme wildfires over northern Greece during summer 2023 – Part A: Effects on aerosol
782 optical properties and solar UV radiation, *Atmospheric Research*, 311, 107700,
783 <https://doi.org/10.1016/j.atmosres.2024.107700>, 2024.
- 784 Min, S. K.: Human influence can explain the widespread exceptional warmth in 2023. *Commun.*
785 *Earth Environ.* 5, 215 <https://doi.org/10.1038/s43247-024-01391-x>, 2024.
- 786 Omar, A. H., Winker, D. M., Vaughan, M. A., Hu, Y., Trepte, C. R., Ferrare, R. A., Lee, K.-P.,
787 Hostetler, C. A., Kittaka, C., Rogers, R. R., Kuehn, R. E., and Liu, Z.: The CALIPSO automated
788 aerosol classification and lidar ratio selection algorithm, *J. Atmos. Ocean. Tech.*, 26, 1994–2014,
789 <https://doi.org/10.1175/2009JTECHA1231.1>, 2009.
- 790 Ou-Yang, C. F., Lin, N. H., Sheu, G. R., Lee, C. T., and Wang, J. L.: Seasonal and diurnal
791 variations of ozone at a high-altitude mountain baseline station in East Asia, *Atmos. Environ.*, 46,
792 279–288, <https://doi.org/10.1016/j.atmosenv.2011.09.060>, 2012.
- 793 Ou-Yang, C. F., Lin, N. H., Lin, C. C., Wang, S. H., Sheu, G. R., Lee, C. Te, Schnell, R. C., Lang,
794 P. M., Kawasato, T., and Wang, J. L.: Characteristics of atmospheric carbon monoxide at a high-
795 mountain background station in East Asia, *Atmos. Environ.*, 89, 613–622,
796 <https://doi.org/10.1016/j.atmosenv.2014.02.060>, 2014.
- 797 Ou-Yang, C. F., Ravindra Babu, S., Lee, J.-R., Yen, M.-C., Griffith, S. M., Lin, C.-C., Chang, S.-
798 C., and Lin, N.-H.: Detection of stratospheric intrusion events and their role in ozone enhancement

799 at a mountain background site in sub-tropical East Asia, *Atmos. Environ.*, 268, 118779,
800 <https://doi.org/10.1016/j.atmosenv.2021.118779>, 2022.

801 Pani, S. K., Wang, S. H., Lin, N. H., Lee, C. Te, Tsay, S. C., Holben, B. N., Janjai, S., Hsiao, T.
802 C., Chuang, M. T., and Chantara, S.: Radiative effect of springtime biomass-burning aerosols over
803 northern Indochina during 7-SEAS/BASELInE 2013 campaign, *Aerosol Air Qual. Res.*, 16, 2802–
804 2817, <https://doi.org/10.4209/aaqr.2016.03.0130>, 2016.

805 Pani, S. K., Ou-Yang, C.-F., Wang, S.-H., Ogren, J. A., Sheridan, P. J., Sheu, G.-R., and Lin, N.-
806 H. J. A. E.: Relationship between long-range transported atmospheric black carbon and carbon
807 monoxide at a high-altitude background station in East Asia, *Atmos. Environ.*, 210, 86–99,
808 <https://doi.org/10.1016/j.atmosenv.2019.04.053>, 2019.

809 Pani, S.K., Huang, H.-Y., Wang, S.-H., Holben, B.N., Lin, N.-H.: Long-term observation of
810 columnar aerosol optical properties over the remote South China Sea. *Sci. Total Environ.* 905,
811 167113 <https://doi.org/10.1016/j.scitotenv.2023.167113>, 2023.

812 Platnick, S., King, M. and Hubanks, P.: MODIS Atmosphere L3 Monthly Product.
813 https://doi.org/10.5067/MODIS/MOD08_M3.006, 2015.

814 Perkins-Kirkpatrick, S., Barriopedro, D., Jha, R., Wang, L., Mondal, A., Libonati, R., and
815 Kornhuber, K.: Extreme terrestrial heat in 2023, *Nature Reviews Earth & Environment*, 5, 244–
816 246, <https://doi.org/10.1038/s43017-024-00536-y>, 2024.

817 Raghuraman, S. P., Soden, B., Clement, A., Vecchi, G., Menemenlis, S., and Yang, W.: The 2023
818 global warming spike was driven by the El Niño–Southern Oscillation, *Atmos. Chem. Phys.*, 24,
819 11275–11283, <https://doi.org/10.5194/acp-24-11275-2024>, 2024.

820 Ramanathan, V., Crutzen, P. J., Kiehl, J. T., and Rosenfeld, D.: Aerosols, climate, and the
821 hydrological cycle, *Science*, 294, 2119–2124, <https://doi.org/10.1126/science.1064034>, 2001.

822 Ravindra Babu, S., Ou-Yang, C.-F., Griffith, S. M., Pani, S. K., Kong, S. S.-K., and Lin, N.-H.:
823 Transport pathways of carbon monoxide from Indonesian fire pollution to a subtropical high-
824 altitude mountain site in the western North Pacific, *Atmos. Chem. Phys.*, 23, 4727–4740,
825 <https://doi.org/10.5194/acp-23-4727-2023>, 2023.

826 Ravindra Babu, S. and Lin, N-H.: Changing pattern of springtime biomass burning over Peninsular
827 Southeast Asia (PSEA) in recent decades. *ESS Open Archive* . August 08, 2023. DOI:
828 10.22541/essoar.169111389.92212046/v2, 2023.

829 Reid, J. S., Hyer, E. J., Johnson, R., Holben, B. N., Yokelson, R. J., Zhang, J., Campbell, J. R.,
830 Christopher, S. A., Di Girolamo, L., Giglio, L., Holz, R. E., Kearney, C., Miettinen, J., Reid, E.
831 A., Turk, F. J., Wang, J., Xian, P., Zhao, G., Balasubramanian, R., Chew, B. N., Janai, S., Lagrosas,
832 N., Lestari, P., Lin, N.-H., Mahmud, M., Nguyen, A. X., Norris, B., Oahn, N. T. K., Oo, M.,
833 Salinas, S. V., Welton, E. J., Liew, S. C.: Observing and understanding the Southeast Asian aerosol
834 system by remote sensing: An initial review and analysis for the Seven Southeast Asian Studies

835 (7SEAS) program, *Atmos. Res.*, 122, 403–468, <https://doi.org/10.1016/j.atmosres.2012.06.005>,
836 2013.

837 Roy, D. P., De Lemos, H., Huang, H., Giglio, L., Houborg, R. and Miura, T.: Multi-resolution
838 monitoring of the 2023 Maui wildfires, implications and needs for satellite-based wildfire disaster
839 monitoring. *Sci. Remote Sens.* 10, 100142. <https://doi.org/10.1016/j.srs.2024.100142>, 2024.

840 Sayer, A. M., Munchak, L. A., Hsu, N. C., Levy, R. C., Bettenhausen, C., and Jeong, M. J.:
841 MODIS collection 6 aerosol products: comparison between Aqua's e-Deep Blue, Dark Target, and
842 “merged” datasets, and usage recommendations, *J. Geophys. Res. Atmos.*, 119, 13965–13989,
843 2014.

844 Seneviratne, S. I., Zhang, X., Adnan, M., Badi, W., Dereczynski, C., Di Luca, A., Ghosh, S.,
845 Iskandar, I., Kossin, J., Lewis, S., Otto, F., Pinto, I., Satoh, M., Vicente-Serrano, S. M., Wehner,
846 M., and Zhou, B.: Weather and Climate Extreme Events in a Changing Climate. In *Proc. Climate*
847 *Change 2021: The Physical Science Basis*. Contribution of Working Group I to the Sixth
848 Assessment Report of the Intergovernmental Panel on Climate Change, 1513–1766 (Cambridge
849 University Press, 2021). <https://doi.org/10.1017/9781009157896.013>, 2021

850 Sheu, G.-R., Lin, N.-H., Wang, J.-L., Lee, C.-T., Ou Yang, C.-F., and Wang, S.-H.: Temporal
851 distribution and potential sources of atmospheric mercury measured at a high-elevation
852 background station in Taiwan, *Atmos. Environ.*, 44, 2393–2400,
853 <https://doi.org/10.1016/j.atmosenv.2010.04.009>, 2010.

854 Sinyuk, A., Holben, B. N., Eck, T. F., Giles, D. M., Slutsker, I., Korkin, S., Schafer, J. S., Smirnov,
855 A., Sorokin, M., and Lyapustin, A.: The AERONET Version 3 aerosol retrieval algorithm,
856 associated uncertainties and comparisons to Version 2, *Atmos. Meas. Tech.*, 13, 3375–3411,
857 <https://doi.org/10.5194/amt-13-3375-2020>, 2020.

858 Torbenson, M. and Büntgen, U.: summer warmth unparalleled over the past 2,000 years. *Nature*
859 631, 94–97 (2024). <https://doi.org/10.1038/s41586-024-07512-y>, 2023.

860 Tsay, S. C., Maring, H. B., Lin, N. H., Buntoung, S., Chantara, S., Chuang, H. C., Gabriel, P. M.,
861 Goodloe, C. S., Holben, B. N., Hsiao, T. C., Christina Hsu, N., Janjai, S., Lau, W. K. M., Lee, C.
862 Te, Lee, J., Loftus, A. M., Nguyen, A. X., Nguyen, C. M., Pani, S. K., Pantina, P., Sayer, A. M.,
863 Tao, W. K., Wang, S. H., Welton, E. J., Wiriyaya, W., and Yen, M. C.: Satellitesurface perspectives
864 of air quality and aerosol-cloud effects on the environment: An overview of 7-SEAS/BASELInE,
865 *Aerosol Air Qual. Res.*, 16, 2581–2602, <https://doi.org/10.4209/aaqr.2016.08.0350>, 2016.

866 Twomey, S.: The Influence of Pollution on the Shortwave Albedo of Clouds, *Journal of*
867 *Atmospheric Sciences*, 34, 1149–1152, [https://doi.org/10.1175/1520-0469\(1977\)034<1149:TIOPOT>2.0.CO;2](https://doi.org/10.1175/1520-0469(1977)034<1149:TIOPOT>2.0.CO;2), 1977.

869 Wang, S., Guan, L., Cohen, J.B., and Qin, K.: Reconstructing top-down global black carbon
870 emissions using remote sensing and models, *Atmospheric Pollution Research*, 16, 10, (102633).
871 <https://doi.org/10.1016/j.apr.2025.102633>, 2025.

872 Wang, S., Cohen, J. B., Deng, W., Qin, K., and Guo, J.: Using a New Top-Down Constrained
873 Emissions Inventory to Attribute the Previously Unknown Source of Extreme Aerosol Loadings
874 Observed Annually in the Monsoon Asia Free Troposphere, *Earths Fut.*, 9, e2021EF002167,
875 <https://doi.org/10.1029/2021EF002167>, 2021.

876 Wang, S., Cohen, J. B., Guan, L., Lu, L., Tiwari, P., & Qin, K.: Observationally constrained global
877 NO_x and CO emissions variability reveals sources which contribute significantly to CO₂
878 emissions, *npj Climate and Atmospheric Science*, 10.1038/s41612-025-00977-2, 8, 1, 2025.

879 Warner, J. X., Comer, M. M., Barnet, C. D., McMillan, W. W., Wolf, W., Maddy, E., and Sachse,
880 G.: A Comparison of Satellite Tropospheric Carbon Monoxide Measurements from AIRS and
881 MOPITT During INTEX-A, *J. Geophys. Res.*, 112, D12S17,
882 <https://doi.org/10.1029/2006JD007925>, 2007.

883 Warner, J., Carminati, F., Wei, Z., Lahoz, W., and Attié, J.-L.: Tropospheric carbon monoxide
884 variability from AIRS under clear and cloudy conditions, *Atmos. Chem. Phys.*, 13, 12469–12479,
885 <https://doi.org/10.5194/acp-13-12469-2013>, 2013.

886 Wai, K. M., Lin, N., Wang, S., and Dokiya, Y.: Rainwater chemistry at a high-altitude station, Mt.
887 Lulin, Taiwan: Comparison with a background station, Mt. Fuji, *J. Geophys. Res.-Atmos.*, 113,
888 D06305, <https://doi.org/10.1029/2006JD008248>, 2008.

889 Wei, J., Li, Z., Peng, Y., and Sun, L.: MODIS Collection 6.1 aerosol optical depth products over
890 land and ocean: validation and comparison, *Atmos. Environ.*, 201, 428–440, 2019a.

891 Wei, J., Li, Z., Sun, L., Peng, Y., and Wang, L.: Improved merge schemes for MODIS Collection
892 6.1 Dark Target and Deep Blue combined aerosol products, *Atmos. Environ.*, 202, 315–327,
893 2019b.

894 Worden, H., Deeter, M., Edwards, D., Gille, J., Drummond, J., and Nédélec, P.: Observations of
895 near-surface carbon monoxide from space using MOPITT multispectral retrievals, *J. Geophys.*
896 *Res.-Atmos.*, 115, D18314, <https://doi.org/10.1029/2010JD014242>, 2010.

897 Xia, L., Liu, R., Fan, W., and Ren, C.: Emerging carbon dioxide hotspots in East Asia identified
898 by a top-down inventory, *Commun. Earth Environ.*, 6, 1–13, [https://doi.org/10.1038/s43247-024-](https://doi.org/10.1038/s43247-024-01991-7)
899 [01991-7](https://doi.org/10.1038/s43247-024-01991-7), 2025.

900 Yadav, I. C., Linthoingambi Devi, N., Li, J., Syed, J. H., Zhang, G., and Watanabe, H.: Biomass
901 burning in Indo-China peninsula and its impacts on regional air quality and global climate change
902 – a review, *Environ. Pollut.*, 227, 414–427, <https://doi.org/10.1016/j.envpol.2017.04.085>, 2017.

903 Zachariah, M., Vautard, R., Chaithra, S. T., Kimutai, J., Arulalan, T., AchutaRao, K., Otto, F. E.
904 L.: Extreme humid heat in South and Southeast Asia in April 2023, largely driven by climate
905 change, detrimental to vulnerable and disadvantaged communities. *World Weather Attribution*.
906 <https://doi.org/10.25561/104092>, 2023.

907 Zeng, Z. and Sun, J.: Impacts of a tripolar sea surface temperature pattern over tropical–North
908 Pacific on interannual variations of spring extreme consecutive dry days over southern China. *J.*
909 *Geophys. Res. Atmos.* 127, e2021JD036281. <https://doi.org/10.1029/2021JD036281>, 2022.

910

911